

Imaging, Therapeutics, and Advanced Technology in Head and Neck Surgery and Otolaryngology 2024

Brian J. F. Wong
Justus F. Ilgner
Editors

27 January 2024
San Francisco, California, United States

Sponsored and Published by
SPIE

Volume 12818

Proceedings of SPIE, 1605-7422, V. 12818

SPIE is an international society advancing an interdisciplinary approach to the science and application of light.

Imaging, Therapeutics, and Advanced Technology in Head and Neck Surgery and Otolaryngology 2024,
edited by Brian J. F. Wong, Justus F. Ilgner, Proc. of SPIE Vol. 12818, 1281801
© 2024 SPIE · 1605-7422 · doi: 10.1117/12.3030018

The papers in this volume were part of the technical conference cited on the cover and title page. Papers were selected and subject to review by the editors and conference program committee. Some conference presentations may not be available for publication. Additional papers and presentation recordings may be available online in the SPIE Digital Library at SPIDigitalLibrary.org.

The papers reflect the work and thoughts of the authors and are published herein as submitted. The publisher is not responsible for the validity of the information or for any outcomes resulting from reliance thereon.

Please use the following format to cite material from these proceedings:
Author(s), "Title of Paper," in *Imaging, Therapeutics, and Advanced Technology in Head and Neck Surgery and Otolaryngology 2024*, edited by Brian J. F. Wong, Justus F. Ilgner, Proc. of SPIE 12818, Seven-digit Article CID Number (DD/MM/YYYY); (DOI URL).

ISSN: 1605-7422
ISSN: 2410-9045 (electronic)

ISBN: 9781510668959
ISBN: 9781510668966 (electronic)

Published by
SPIE
P.O. Box 10, Bellingham, Washington 98227-0010 USA
Telephone +1 360 676 3290 (Pacific Time)
SPIE.org
Copyright © 2024 Society of Photo-Optical Instrumentation Engineers (SPIE).

Copying of material in this book for internal or personal use, or for the internal or personal use of specific clients, beyond the fair use provisions granted by the U.S. Copyright Law is authorized by SPIE subject to payment of fees. To obtain permission to use and share articles in this volume, visit Copyright Clearance Center at copyright.com. Other copying for republication, resale, advertising or promotion, or any form of systematic or multiple reproduction of any material in this book is prohibited except with permission in writing from the publisher.

Printed in the United States of America by Curran Associates, Inc., under license from SPIE.

Publication of record for individual papers is online in the SPIE Digital Library.

SPIE. DIGITAL LIBRARY
SPIDigitalLibrary.org

Paper Numbering: A unique citation identifier (CID) number is assigned to each article in the Proceedings of SPIE at the time of publication. Utilization of CIDs allows articles to be fully citable as soon as they are published online, and connects the same identifier to all online and print versions of the publication. SPIE uses a seven-digit CID article numbering system structured as follows:

- The first five digits correspond to the SPIE volume number.
- The last two digits indicate publication order within the volume using a Base 36 numbering system employing both numerals and letters. These two-number sets start with 00, 01, 02, 03, 04, 05, 06, 07, 08, 09, 0A, 0B ... 0Z, followed by 10-1Z, 20-2Z, etc. The CID Number appears on each page of the manuscript.

Contents

v *Conference Committee*

FROM OUTER EAR TO THE COCHLEA: ADVANCED IMAGING BY OCT AND ITS MODIFICATIONS

12818 02 **Analysis of ear symmetry as a diagnostic tool enabled by optical coherence tomography**
[12818-1]

DETECTING MALIGNANCY OF THE UPPER AERODIGESTIVE TRACT AND ITS MARGINS BY MEANS OF MULTIMODAL IMAGING

12818 03 **Cutaneous melanoma detection via dynamic optical contrast imaging** [12818-14]

ADVANCED PHOTONICS FOR TARGETED ONCOTHERAPY AND THERAPEUTIC MONITORING

12818 04 **A rapid spectroscopic platform in identifying cisplatin resistance in head and neck squamous cell carcinoma** [12818-15]

12818 05 **Photobiomodulation therapy for the management of oral mucositis: a clinical case** [12818-17]

STRUCTURAL ASSESSMENT AND ROBOTICS IN HEAD AND NECK SURGERY

12818 06 **Intraoral scanner and stereographic 3D print in prosthodontics: three-year evaluation of in vitro and in vivo approaches** [12818-20]

POSTER SESSION

12818 07 **Optical imaging modalities for the detection of head and neck cancer margins** [12818-26]

12818 08 **Development of an augmented reality system for tracheal intubation guidance of airway management** [12818-9]

Conference Committee

Symposium Chairs

Sergio Fantini, Tufts University (United States)
Paola Taroni, Politecnico di Milano (Italy)

Program Track Chairs

Brian Jet-Fei Wong, Beckman Laser Institute and Medical Clinic
(United States) and University of California, Irvine (United States)
Eva M. Sevick, The University of Texas Health Science Center at
Houston (United States)

Conference Chairs

Brian Jet-Fei Wong, Beckman Laser Institute and Medical Clinic
(United States) and University of California, Irvine (United States)
Justus F. Ilgner, Universitätsklinikum Rheinisch-Westfälische Technische
Hochschule Aachen (Germany)

Conference Program Committee

Javier A. Jo, The University of Oklahoma (United States)
Milind Rajadhyaksha, Memorial Sloan-Kettering Cancer Center
(United States)
Amy L. Oldenburg, The University of North Carolina at Chapel Hill
(United States)
Ramesh K. Shori, Naval Undersea Warfare Center Keyport
(United States)

Analysis of ear symmetry as a diagnostic tool enabled by Optical Coherence Tomography

Zihan Yang^a, Wihan Kim^a, Marcela A. Morán^a, Ryan Long^a, John S. Oghalai^{a,b}, and Brian E. Applegate^{a,b,*}

^aUniversity of Southern California, Caruso Department of Otolaryngology–Head & Neck Surgery, Los Angeles, CA

^bUniversity of Southern California, Alfred Mann Department of Biomedical Engineering, Los Angeles, CA

ABSTRACT

Early diagnosis of ear disorders is difficult in part because patients do not seek out an otologist until they have significant hearing loss. Early detection could happen in the primary care provider's office, however the sensitivity of an otoscopic examination by a primary care provider during an annual physical is very low. On the other hand, Optical Coherence Tomography (OCT) imaging of the tympanic membrane and middle ear can provide detailed volumetric images of the structure and function. These detailed images can form the basis for an approach for finding early signs of ear disease. Our hypothesis is that asymmetry between the ears could be used for early diagnosis.

In order to test this, we need to understand the naturally occurring asymmetry in healthy volunteers. We have collected volumetric OCT images from 8 healthy subjects using a hand-held otoscopic OCT system. As part of a registration algorithm, we crop and down sample the data before finding the transformation matrix that registers the volumes. This matrix is then used to register the original volumes. Then the quantitative analysis of the symmetry between the left and right ears was applied through the similarity coefficient and overall, the left and right ears similarity of 8 healthy subjects has a mean of 0.7892, and a standard deviation of 0.0186.

From a scientific perspective, this is the first quantitative measure of how symmetric the right and left ears are in humans. From a diagnostic perspective, this approach could provide a simple method to find early signs of ear disease.

Keywords: optical coherence tomography, otology, registration, symmetry, quantitative analysis

1. INTRODUCTION

Early diagnosis of ear disorders is important to prevent patients from developing significant hearing loss¹. However, the traditional otoscope and surgical microscope have several weaknesses, even though they are essential visualization tools for the otolaryngologist². Usually, otoscopy can provide visualization of just the lateral surface of the tympanic membrane (TM). Deeper middle ear (ME) structures, such as the stapes, are not detected, making the diagnosis less accurate³. Some auxiliary tools, such as computed tomography (CT) and magnetic resonance imaging (MRI), are currently used for pathological examination of ME⁴. Even though CT performs excellently on bone abnormalities, it performs poorly on soft tissue differences and carries the risk of radiation exposure. MRI is suitable for soft tissue examination, but the spatial resolution is insufficient to clearly visualize ME and is not suitable for patients with metallic implants.

OCT is a non-invasive imaging technique that allows real-time, high-resolution imaging of microstructures and has been widely used in ophthalmology^{5,6}. In otology, OCT also has been proved to have the potential to apply to the clinic, especially in TM and ME, with the advantage of imaging resolution and depth⁷⁻¹¹. Equipped with the handheld otologic probe, OCT enables imaging of ear anatomy in humans². OCT imaging of the TM has been used for diagnosis of otitis media (OM), where chronic OM can be diagnosed by the detection of biofilm behind the TM^{12,13}. In addition, the previous studies have been demonstrated TM thickness is a proposed metric to differentiate normal, chronic and acute otitis media infections^{14,15}. Using OCT to detect middle ear effusions was achieved with a high accuracy of 90.6%¹⁶. Additionally, important progress has been made in the adaptation of OCT to differentiate cholesteatoma from normal ME mucosa¹⁷. Although OCT has been widely used to study of TM and ME, there are no comprehensive evaluation parameters to support

the quantitative study of ear anatomy, which is very important for further implementation of quantitative pathological diagnosis.

In addition, the knowledge of ear symmetry is crucial for assessing the structural development of children's ears, evaluating early otologic lesions and even for the design of hearing aid instruments. Fu et al. evaluated the morphological variations of the entire three dimensional (3D) external ear with a parameterized 3D ear modelling¹⁸. Claes et al. investigated the matching symmetry in anatomical substructures of the human pinnae by using 3D spatially dense geometric morphometrics, which have important implications on ear recognition and sound localization¹⁹. While the studies in external ear dimensions, position and symmetry have been reported, the symmetry on middle ear has not been studied so far²⁰⁻²².

To provide a simple method to investigate early signs of ear disease, in this paper, we performed quantitative analysis of the left and right ears symmetry where the 3D datasets were registered after being acquired by a customized handheld otologic OCT system.

2. METHODS

2.1 Hand-held otoscopic OCT system and data correction

A customized hand-held OCT system was developed for middle ear imaging. The swept source has a central wavelength of 1310 nm, a bandwidth of 39 nm, and a sweep rate of 200KHz, which can achieve rapid scanning of middle ear morphological structures in clinical practice. The system integrates a small visible light CMOS sensor and is therefore capable of simultaneous OCT scanning and otoscope imaging.

A total of eight healthy subjects' ears were imaged by our handheld otology OCT system, with multiple OCT volumetric data collected for each subject. Thanks to the integrated live video sensor, the scanning position can be easily located, and the corresponding middle ear structures can be clearly observed in the OCT images. Total imaging time was less than 5 minutes per ear.

2.2 3D Registration

To achieve quantitative symmetry analysis of the left and right ears, image registration must first be performed. Considering the differences in the position and angle of the handheld probe during the imaging process, registration based on 3D OCT images is necessary. As shown in Fig. 1, according to the chiral structure of the left and right ears, the OCT volumetric data of the left ear is first flipped left and right. To reduce registration time and improve registration accuracy, image cropping is applied to remove redundant background. Further, in order to speed up the registration process, the left and right ear data are down sampled. Depending on the data size and registration accuracy requirements, an appropriate down sampling rate can be selected. In this paper, 4x down sampling is applied by balancing registration accuracy and time. The preprocessed data is used for 3D data registration.

Here, according to our application scenario, an OCT volumetric data registration method based on multiple 2D images is applied. As mentioned above, to reduce the difference in imaging position and angle, the enface images (XY plane) of the left and right ear data are first registered. Then, two separate registrations are performed in the XZ plane and the YZ plane. The three transformation matrices obtained are then combined into the final transformation matrix. By applying it to the original volumetric data, the final registration result is obtained.

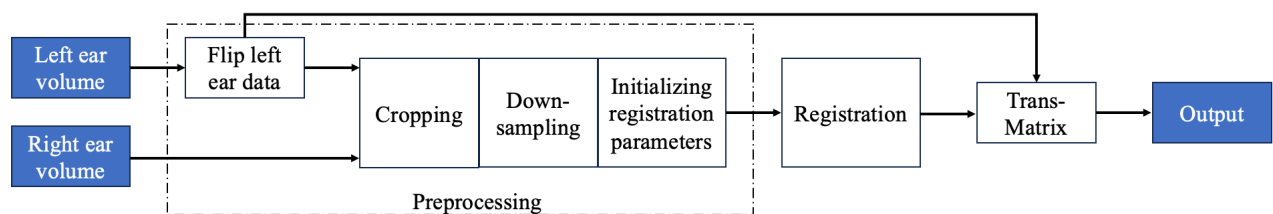


Figure 1. Working flow of the left and right ears registration.

2.3 Symmetry analysis

A measurement method based on DICE similarity coefficient (DSC) is used to evaluate the symmetry of the left and right ears. DSC is a scale in 0 to 1, where a DSC value of 1 indicates the overlap between left and right ears are a perfect match. First, each B-scan image pairs are sequentially extracted from the two registered 3D datasets where the B-scan images are at the same position of the left and right ears. Then, binarization process is performed to extract the middle ear tissue area of image pairs. According to Eq. 1, the DICE coefficient at the same position is calculated as the similarity measurement result. Finally, volume symmetry is represented by the overall average of the similarity coefficients of each B-scan.

$$DICE(A_{left}, A_{right}) = \frac{2(A_{left} \cap A_{right})}{A_{left} \cup A_{right}} \quad (1)$$

Where A_{left} is the area of one B-scan image in the left ear and A_{right} is the area of the B-scan image in the corresponding position of the right ear.

3. RESULTS

3.1 OCT images acquired from our otoscopic OCT system

Otoscope images and corresponding OCT images are shown in Fig. 2. A volume scan is performed after determining the scanning position from the otoscope image. The top row shows the camera image, 3D reconstructed OCT images and one B-scan image, from the left ear. The bottom row shows the corresponding images of the right ear. The middle ear structures can be clearly observed from the OCT images.

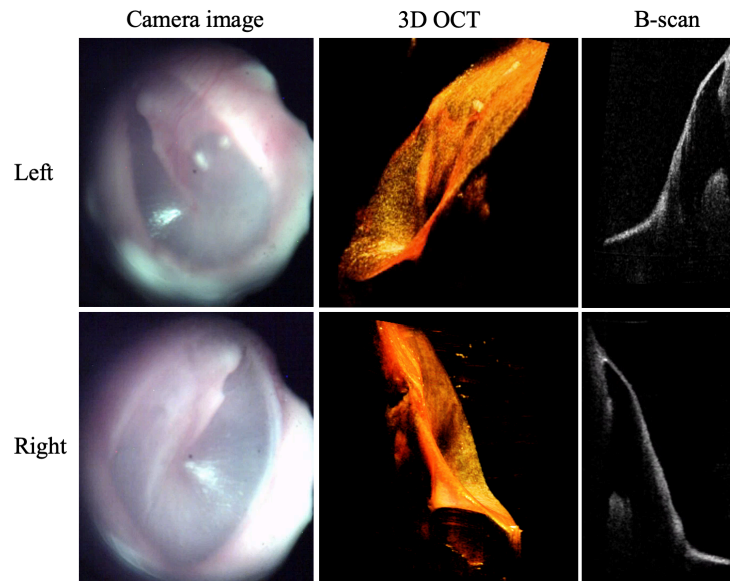


Figure 2 Otoscope images and corresponding OCT images obtained from the customized handheld otology OCT system.

3.2 3D registration

According to the registration process in Section 2.2, the 3D OCT images of the left and right ears were registered. Figure 3 shows the representative registration results of 3D OCT images of the left and right ears, where the red represents the OCT images of the left ear, while the green represents the OCT images of the right ear. Three cross-sections including XZ plane, YZ plane and XY plane are shown in Figs. 3 (a)-(c), respectively. Figure 3 (d) shows the 3D reconstructed registration results. Qualitatively, OCT images of the left and right ears match well.

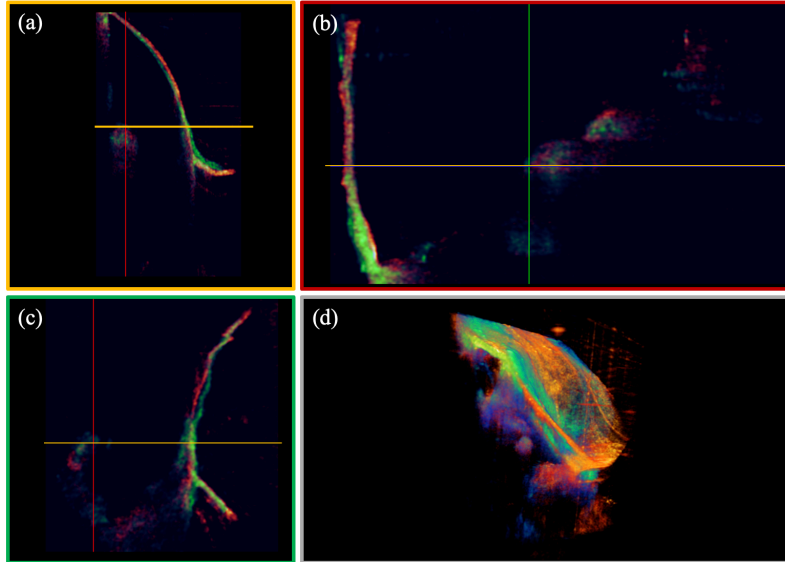


Figure 3 Registration results of 3D OCT images between the left and right ears. (a) 2D images in XZ plane. (b) 2D images in YZ plane. (c) 2D images in XY plane. (d) 3D registration.

3.3 Symmetry results

After registering the 3D OCT images of the left and right ears, quantitative analysis based on volume similarity was performed. Figure 4 shows the left and right ear symmetry results of 8 healthy subjects. Overall, the left and right ears similarity of 8 healthy subjects has a mean of 0.7892, and a standard deviation of 0.0186.

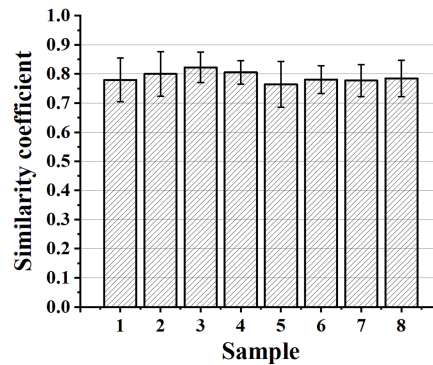


Figure 4 Quantitative results between left and right ear symmetry in healthy subjects.

4. DISCUSSION AND CONCLUSION

Early diagnosis of ear diseases has always been one of the research topics that clinicians and researchers are committed to. Inspired by the perfect symmetry of chiral structures, asymmetry between the ears could be used for early diagnosis.

To the best of our knowledge, it is the first report of symmetry in the middle ear. In this paper, we first used the customized handheld otology OCT system combined with a real-time CMOS sensor to image the middle ears of 8 healthy subjects. Secondly, in order to compensate for the difference in imaging position and angle of the handheld probe during the imaging process, 3D image registration was performed. Then the quantitative analysis of the symmetry between the left and right ears was applied through the similarity coefficient and overall, the left and right ears similarity of 8 healthy subjects has a mean of 0.7892, and a standard deviation of 0.0186.

This study still has some limitations. First, due to the limited imaging range of the scanning probe, it is impossible to image the entire TM. In response to this limitation, we are working on OCT volume stitching through multiple scans, aiming to achieve complete TM imaging and quantitative analysis. Secondly, the number of subjects involved was limited. In order to establish more accurate symmetry evaluation criteria, a larger number of subjects is necessary.

This work provides a new research direction for the diagnosis of ear diseases, especially early detection, through the quantitative evaluation of left and right ear symmetry. In future, we will continue to recruit more patients to evaluate the asymmetry of diseased ears.

REFERENCES

- [1] Ptok, M., "Early detection of hearing impairment in newborns and infants", *Dtsch Arztebl Int*, 108(25), 426-431 (2011)
- [2] Lui, C.G., Kim, W., Dewey, J.B., Macias-Escriba, F.D., Ratnayake, K., Oghalai, J.S., and Applegate, B.E., "In vivo functional imaging of the human middle ear with a hand-held optical coherence tomography device", *Biomedical optics express*, 12(8), 5196-5213 (2021)
- [3] Blomgren, K., and Pitkäranta, A., "Current challenges in diagnosis of acute otitis media", *Int J Pediatr Otorhinolaryngol*, 69(3), 295-299 (2005)
- [4] Trojanowska, A., Drop, A., Trojanowski, P., Rosinska-Bogusiewicz, K., Klatka, J., and Bobek-Billewicz, B., "External and middle ear diseases: radiological diagnosis based on clinical signs and symptoms", *Insights Imaging*, 3(1), 33-48 (2012)
- [5] Carrasco-Zevallos, O.M., Viehland, C., Keller, B., Draelos, M., Kuo, A.N., Toth, C.A., and Izatt, J.A., "Review of intraoperative optical coherence tomography: technology and applications [Invited]", *Biomedical optics express*, 8(3), 1607-1637 (2017)
- [6] Everett, M., Magazzeni, S., Schmoll, T., and Kempe, M., "Optical coherence tomography: From technology to applications in ophthalmology", *Translational Biophotonics*, 3(1)(2020)
- [7] Pitris, C., Saunders, K.T., Fujimoto, J.G., and Brezinski, M.E., "High-Resolution Imaging of the Middle Ear With Optical Coherence Tomography: A Feasibility Study", *Archives of Otolaryngology-Head & Neck Surgery*, 127(6), 637-642 (2001)
- [8] Tan, H.E.I., Santa Maria, P.L., Wijesinghe, P., Francis Kennedy, B., Allardyce, B.J., Eikelboom, R.H., Atlas, M.D., and Dilley, R.J., "Optical Coherence Tomography of the Tympanic Membrane and Middle Ear: A Review", *Otolaryngol Head Neck Surg*, 159(3), 424-438 (2018)
- [9] Cho, N.H., Jang, J.H., Jung, W., and Kim, J., "In vivo imaging of middle-ear and inner-ear microstructures of a mouse guided by SD-OCT combined with a surgical microscope", *Optics express*, 22(8), 8985-8995 (2014)
- [10] MacDougall, D., Rainsbury, J., Brown, J., Bance, M., and Adamson, R., "Optical coherence tomography system requirements for clinical diagnostic middle ear imaging", *Journal of biomedical optics*, 20(5), 56008 (2015)
- [11] Burwood, G.W.S., Fridberger, A., Wang, R.K., and Nuttall, A.L., "Revealing the morphology and function of the cochlea and middle ear with optical coherence tomography", *Quant Imaging Med Surg*, 9(5), 858-881 (2019)
- [12] Nguyen, C.T., Tu, H., Chaney, E.J., Stewart, C.N., and Boppart, S.A., "Non-invasive optical interferometry for the assessment of biofilm growth in the middle ear", *Biomedical optics express*, 1(4), 1104-1116 (2010)
- [13] Nguyen, C.T., Robinson, S.R., Jung, W., Novak, M.A., Boppart, S.A., and Allen, J.B., "Investigation of bacterial biofilm in the human middle ear using optical coherence tomography and acoustic measurements", *Hear Res*, 301, 193-200 (2013)
- [14] Cho, N.H., Lee, S.H., Jung, W., Jang, J.H., and Kim, J., "Optical coherence tomography for the diagnosis and evaluation of human otitis media", *J Korean Med Sci*, 30(3), 328-335 (2015)
- [15] Monroy, G.L., Shelton, R.L., Nolan, R.M., Nguyen, C.T., Novak, M.A., Hill, M.C., McCormick, D.T., and Boppart, S.A., "Noninvasive depth-resolved optical measurements of the tympanic membrane and middle ear for differentiating otitis media", *The Laryngoscope*, 125(8), E276-282 (2015)
- [16] Preciado, D., Nolan, R.M., Joshi, R., Krakovsky, G.M., Zhang, A., Pudik, N.A., Kumar, N.K., Shelton, R.L., Boppart, S.A., and Bauman, N.M., "Otitis Media Middle Ear Effusion Identification and Characterization Using an Optical Coherence Tomography Oscope", *Otolaryngol Head Neck Surg*, 162(3), 367-374 (2020)
- [17] Djalilian, H.R., Rubinstein, M., Wu, E.C., Naemi, K., Zardouz, S., Karimi, K., and Wong, B.J., "Optical coherence tomography of cholesteatoma", *Otol Neurotol*, 31(6), 932-935 (2010)
- [18] Fu, F., Luximon, A., and Luximon, Y., "3D human ear modelling with parameterization technique and variation analysis", *Ergonomics*, 1-12 (2023)

- [19] Claes, P., Reijnen, J., Shriver, M.D., Snyders, J., Suetens, P., Nielandt, J., De Tre, G., and Vandermeulen, D., “An investigation of matching symmetry in the human pinnae with possible implications for 3D ear recognition and sound localization”, *J Anat*, 226(1), 60-72 (2015)
- [20] Coward, T.J., Scott, B.J.J., Watson, R.M., and Richards, R., “Laser scanning of the ear identifying the shape and position in subjects with normal facial symmetry”, *International journal of oral and maxillofacial surgery*, 29(1), 18-23 (2000)
- [21] Sforza, C., Grandi, G., Binelli, M., Tommasi, D.G., Rosati, R., and Ferrario, V.F., “Age- and sex-related changes in the normal human ear”, *Forensic Sci Int*, 187(1-3), 110 e111-117 (2009)
- [22] Meijerman, L., Van Der Lugt, C., and Maat, G.J., “Cross - sectional anthropometric study of the external ear” , *Journal of forensic sciences*, 52(2), 286-293 (2007)

Cutaneous melanoma detection via dynamic optical contrast imaging

Lauran Evans*¹, Ethan Han¹, Clare Moffatt¹, Yazeed Alhiyari¹, Solymar Torres¹,
Maddie Doi¹, Brandon Mo¹, Jenny Kim², Ramesh Shori¹, Maie St. John¹

¹David Geffen School of Medicine at UCLA – Department of Head & Neck Surgery; 757 Westwood Blvd, Los Angeles, CA, USA 90095. ²David Geffen School of Medicine at UCLA –Department of Dermatology; 757 Westwood Blvd, Los Angeles, CA, USA 90095.

*LKEvans@mednet.ucla.edu

ABSTRACT

Dynamic optical contrast imaging (DOCI) is an imaging method utilizing fluorescence lifetime that our team has developed for identification of margins in head & neck mucosal malignancies. In this paper we demonstrate the first utilization of DOCI in cutaneous melanoma. We utilized both a 530/30nm band pass filter, as well as a 400nm long pass filter to capture the autofluorescence of tissue fluorophores, after excitation with a 365nm wide field LED light source. Imaging was captured, processed via an established protocol in MatLab, and regions of interest were compared to corresponding histopathology. Patients with biopsy confirmed cutaneous melanoma who were undergoing surgical removal of their malignancy were recruited for in-vivo pre-operative DOCI imaging, intraoperative imaging, then ex-vivo imaging of the tumor after removal. Patients free of disease with benign moles were also recruited for in-vivo DOCI imaging to serve as controls. 11 patients with melanoma and 10 controls were included. DOCI distinguishes between melanoma vs. normal surrounding skin (sensitivity=94% specificity=88%, AUC=0.921) as well as benign nevi vs. melanoma (sensitivity=100% and specificity=80%, AUC=0.953), posing benefit opportunities for both melanoma diagnostics as well as margin determination.

Keywords: melanoma, cutaneous melanoma, margin, nevi, fluorescence lifetime, DOCI, dynamic optical contrast imaging

1. INTRODUCTION

The incidence of cutaneous melanoma has continued to rise over the past two decades without a decrease in mortality rates, and 97,610 people are expected to be diagnosed with melanoma in 2023.¹⁻³ Melanoma is highly curable in the localized stage, thus early detection and complete resection of melanoma remains essential in improving survival.^{4,5} However, current methods for skin cancer detection have their limitations despite advancements in medical technology. One of the main challenges lies in that visual assessment remains the primary method for the initial detection of melanoma.⁶ Providers rely on their expertise and experience to differentiate between benign and malignant skin growths, sending suspicious lesions for biopsy. However, this process is subjective and prone to human error, with studies reporting the sensitivity of visual diagnosis at 81-100% by dermatologists and 42-100% by general practitioners.⁷

Additionally, melanoma can be difficult to detect visually using traditional visual heuristics, especially in early stages when skin changes may be subtle or in certain subtypes such as amelanotic and nodular melanomas⁸. Dermoscopy can increase sensitivity and accuracy of visual screening by allowing specialists to visualize lesions for atypical dermoscopic structures and patterns associated with malignancy, but is likewise subject to human error.^{9,10} Dermoscopy is usually only administered by select trained specialists, such as dermatologists. Additionally, the presence of other skin conditions and anatomical factors can sometimes obscure or mimic signs of skin cancer, further complicating the diagnostic process.^{11,12}

Obtaining clear surgical margins in melanoma resection significantly reduces recurrence and risk of metastasis.^{13,14} However unlike in squamous or basal cell carcinomas, Mohs micrographic surgery is less reliable for melanoma resection, as melanocytes can be altered or obscured in frozen sections.¹⁵⁻¹⁷ Consequently, wide local excision with permanent sections is often employed, a process that may take 1-2 weeks for pathology results. Even then, up to 23% of resected melanomas in the head and neck region return with positive margins, compared to less than 7% in the trunk and proximal extremities.¹⁸ This likely stems from non-compliance with recommended excision margins in hopes of preserving functionality and cosmetic appearance. Thus, a method to assess intraoperative margins would greatly assist surgeons in ensuring complete resection without excessive tissue removal.

Dynamic optical contrast imaging (DOCI) is an imaging modality that our group has developed and utilized for identification of margins in head & neck mucosal malignancies, as well as vocal cord scarring and parathyroid adenoma.¹⁹⁻²² DOCI utilizes a pulsed, ultraviolet light to excite endogenous fluorophores, capturing the natural autofluorescence of tissues in-vivo and ex-vivo. Temporal fluorescence decay differs between tissue types, including malignant and benign tissue. By comparing the fluorescence decay between the excitation and emission states, DOCI generates a spatial map of tissue autofluorescence without the use of complicated algorithms or lengthy image acquisition times, allowing for real-time expedient clinical use.²³ Our team has developed a portable DOCI technique that obtains images in the operating room (OR), in-vivo and ex-vivo, with an imaging time of less than 1 minute.

In this study, we demonstrate the multifaceted utilities of DOCI in cutaneous melanoma: for detection of melanoma compared to benign nevi and surrounding tissue, as well as intraoperative identification of positive margins in patients undergoing surgical excision. In doing so, our group hopes to improve accuracy and accessibility of melanoma screening, while improving survival and quality of life – paving the way for advanced precision surgery in all patients with cutaneous melanoma.

2. METHODS

IRB approval was obtained for this study. Adult patients with biopsy-confirmed cutaneous melanoma in the head and neck region, who were to undergo surgical excision, were recruited for this study. These patients were brought to the OR, and the melanoma lesion was identified by the surgeon. The area around the melanoma was shaven and gently cleaned with alcohol swabs, then let dry. The DOCI machine was then utilized to obtain in-vivo images of the lesion and surrounding skin in the OR, prior to excision of the lesion. Red Green Blue (RGB) photos were also obtained at this time for image mapping and comparison. The melanoma tumors were surgically excised via wide local excision according to clinical standard of care. After the specimen was removed, DOCI images were obtained of the gross ex-vivo specimen on the external skin side, as well as the internal underside of the specimen. Additionally, healthy volunteers with no known history of cutaneous malignancy were recruited for the study. Cutaneous nevi of the volunteers were DOCI imaged in-vivo, along with RGB imaging for comparison. These benign cutaneous lesions were not surgically removed.

Filters of the DOCI device are grouped into different channels based on the range of wavelengths detected with that specific filter, and 5 distinct channels were used to capture DOCI values for each specimen. Channel 5 represents a 580/30nm band pass filter (BPF) and has been utilized in previous studies for identification of mucosal malignancies, thus Channel 5 was explored for detection of melanoma in this study. Upon exploratory data collection, Channel 1 was also found to be useful for examination of melanotic lesions. Channel 1 represents a long pass filter (LPF) at 400nm. Both Channel 1 and Channel 5 were investigated as potential filters for identification of melanoma. However, example images in this study are demonstrated utilizing Channel 1 due to slightly improved visual contrast seen in Channel 1 on preliminary exploration. Post-processing of the images was performed in MatLab based on prior defined DOCI protocols developed by our laboratory, and includes intensity filtering. K-space clustering (3 clusters) was performed, which groups statistically

similar pixels of images together delineating optical differences. This technique assigns a false color to each of the pixel groupings for discrimination purposes. Regions of interest (ROI) were identified on RGB images via two separate clinician reviewers. One patient was excluded from analysis due to poor image quality.

Statistical analyses included univariate logistic regression for comparisons of DOCI values between patients with melanoma vs. nevus, as well as paired t-test for skin vs. melanoma within-subject. Receiver operator curve (ROC) models were constructed to predict detection of melanoma via DOCI, when compared to both surrounding skin and to benign nevus. Models were created utilizing both channels of interest described above, Channel 1 and Channel 5. Sensitivity, specificity, and AUC of DOCI for detection of melanoma were then calculated. Likelihood ratio testing was performed for each variable within the ROC model. Significance was set at $\alpha = 0.05$, and analysis was performed via JMP: Statistical Software (Version 17.0).

3. RESULTS

3.1 Clinical characteristics

11 patients with biopsy-proven cutaneous melanoma were included for DOCI imaging before, during, and after surgical resection. 10 benign nevus control image sets were obtained from healthy volunteers. Among the patients with melanoma, mean Breslow depth measured 3.41mm, with 2 of the 11 cutaneous melanoma patients harboring in-situ lesions. 2 patients demonstrated lentigo maligna, while the remainder of the patients had unspecified melanoma types expressed in the final pathology report. 3 patients had positive or close margins on the main excision specimen, and the remainder had negative margins on the main specimen. None of the patients exhibited evidence of distant metastases.

3.2 Melanoma vs. Surrounding Skin

When comparing the DOCI value between melanoma to surrounding skin within-subject, there was a mean difference of 0.044 (95% CI = 0.014, 0.075) with t-Ratio=3.06, $p=0.0074$. **Figure 1** demonstrates in-vivo images of DOCI (Channel 1), with visual differentiation of melanoma from surrounding skin, and from surrounding tissue such as scabbing from a second prior biopsy site.

The ROC model described in the above methods demonstrated the predictive ability of Channel 1 ($p<0.0001$) and Channel 5 ($p=0.0202$) to detect melanoma vs. surrounding skin. Within this predictive model, DOCI accurately identifies melanoma vs. surrounding skin with sensitivity=94% and specificity=88% (AUC=0.921). This ROC model is demonstrated in **Figure 2A**.

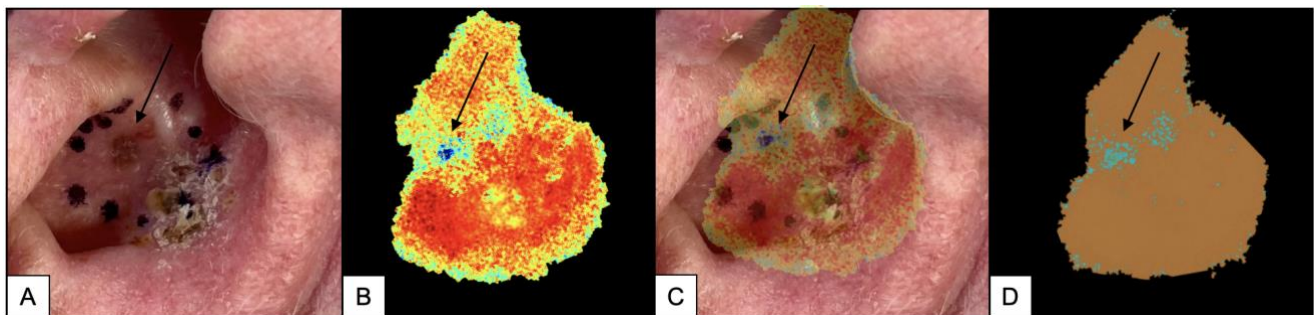


Figure 1. In-vivo DOCI imaging of a right ear melanoma: A) RGB image of right ear with labels. B) DOCI image (Channel 1) with arrow pointing to melanoma area. C) Overlay of DOCI atop RGB, with arrow pointing to melanoma. D) K-space clustering of DOCI imaging, with arrow pointing to melanoma.

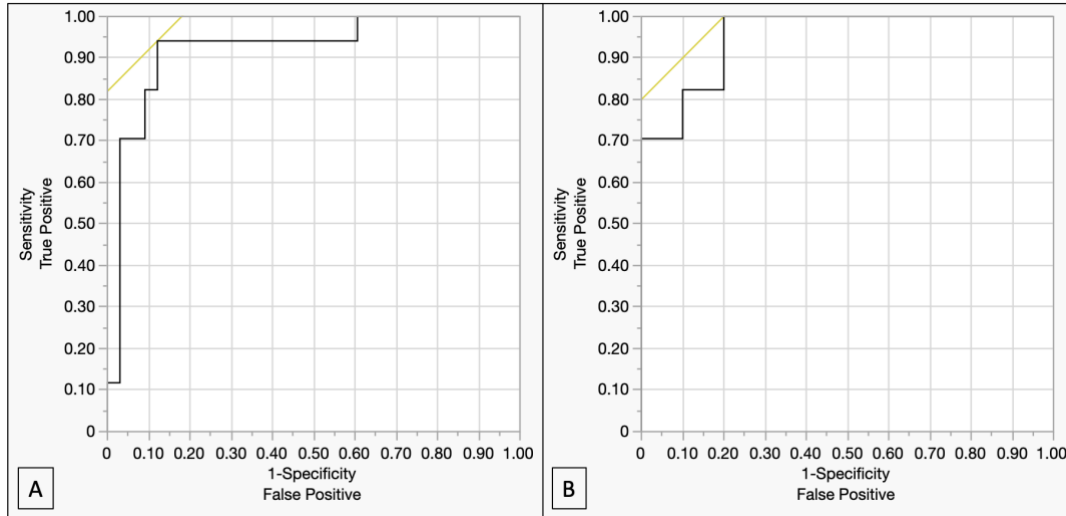


Figure 2. Receiver Operator Curves (ROC) for DOCI melanoma detection. A) ROC of DOCI value to differentiate melanoma vs. surrounding skin, with sensitivity=94% specificity=88%, and AUC=0.921. B) ROC of DOCI value to distinguish melanoma vs. nevus, with sensitivity=100% and specificity=80%, and AUC=0.953.

3.3 Margin Detection

In one case, a positive lateral melanoma margin was identified on DOCI in a freshly excised ex-vivo specimen prior to pathologic review. This positive margin was not visible to the naked eye nor on RGB imaging, but was visible on DOCI imaging in the OR in real-time. DOCI imaging of this lateral positive margin is compared against a different patient's specimen who had negative margins. Ex-vivo melanoma specimen images in **Figure 3** compare RGB images, DOCI images (Channel 1), and corresponding K-space clustering, for visual distinction of positive vs. negative margins.

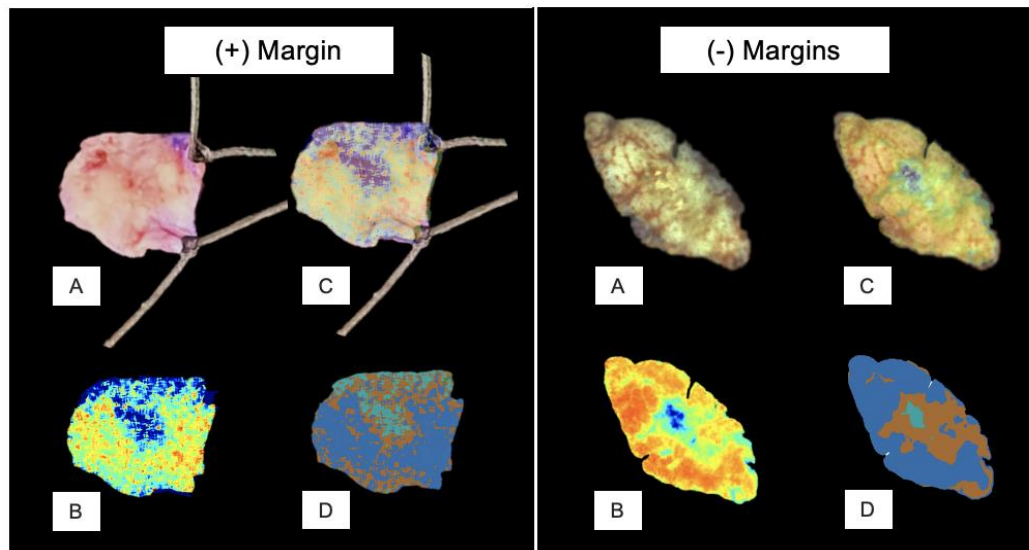


Figure 3. Cutaneous melanoma ex-vivo margin detection. A) RGB photo; B) DOCI image (Channel 1, dark blue = melanoma); C) DOCI overlay onto RGB; D) K-space cluster image (teal = melanoma). The left depicts a (+) margin on the ex-vivo specimen, denoted with an arrow, where dark blue (B) and teal (D) melanoma extends to superior specimen edge. The right depicts (-) margins around the melanoma, whereby dark blue (B) and teal (D) do not extend to specimen edge. Margin status confirmed via pathology.

3.4 Melanoma vs. Nevi

Mean DOCI value among benign nevi was 0.386 (STD=0.041) and among melanoma was 0.314 (STD=0.057). Univariate regression of DOCI value compared between melanoma and nevi results in $X^2=5.46$, $p=0.0195$. **Figure 4** demonstrates the distribution of DOCI data between groups, with improved distinction of melanoma vs. nevi and melanoma vs. surrounding skin when utilizing Channel 1 (over Channel 5). **Figure 5** visually demonstrates in-vivo DOCI recognition of a patient with a nevus vs. a patient with melanoma, as well as differentiation of the melanoma vs. surrounding skin. Due to similarities in DOCI value between nevus and skin, the bottom of Figure 5 demonstrates a non-significant difference on DOCI imaging and K-clustering.

The ROC model demonstrated DOCI's ability to detect melanoma vs. nevi in Channel 1 ($p=0.0176$), but not in Channel 5 ($p=0.1537$). With this predictive model, DOCI accurately identifies melanoma vs. surrounding skin with sensitivity=100% and specificity=80% (AUC=0.953). This ROC for DOCI's ability to determine melanoma vs. nevi is shown in **Figure 2B**.

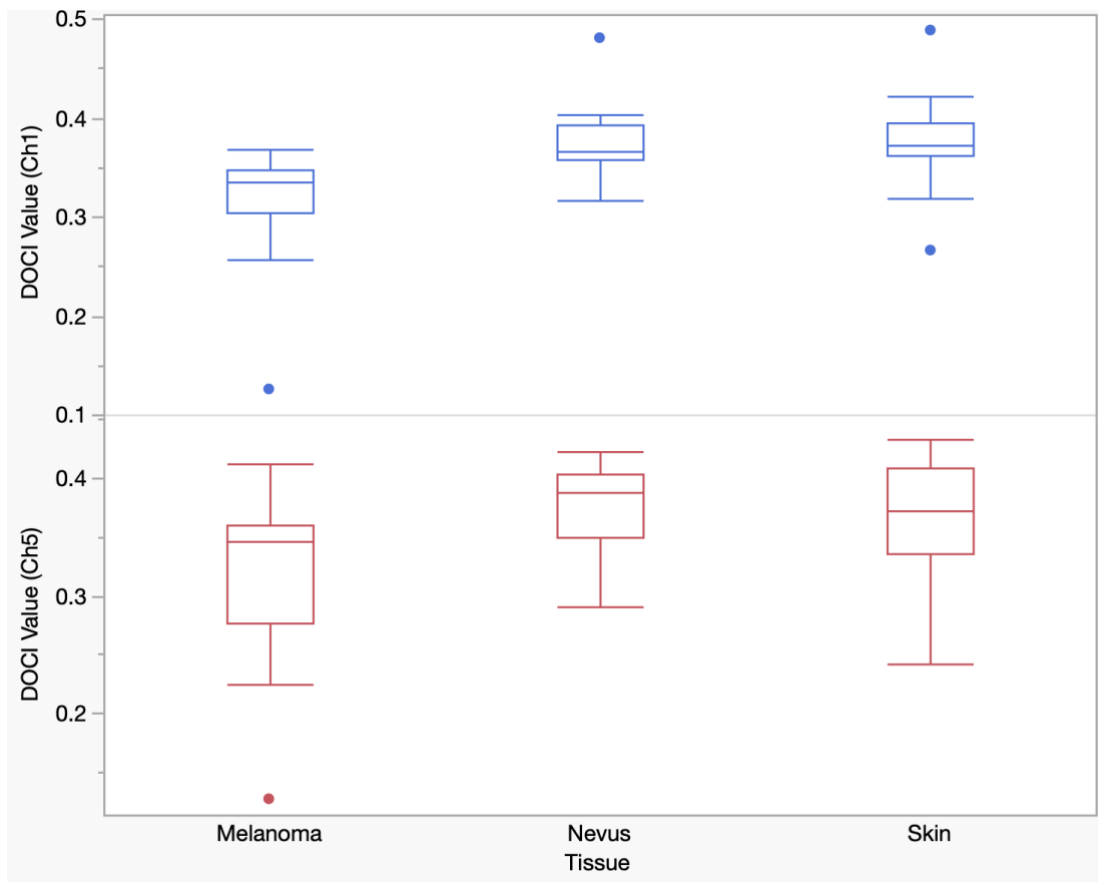


Figure 4. DOCI Values of tissue types. Melanoma, benign nevus, and skin DOCI values are compared to each other via histograms, in Channel 1 (Ch1) and Channel 5 (Ch5). Skin and nevus demonstrate higher DOCI value than melanoma.

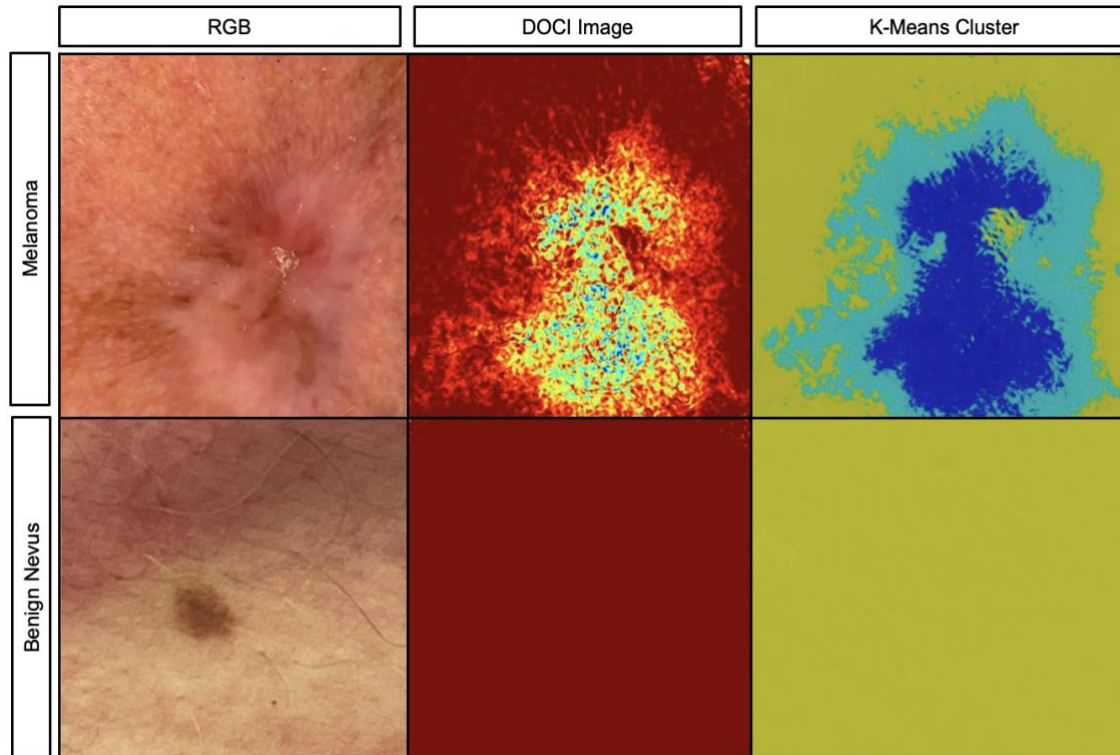


Figure 5. In-vivo identification of melanoma (top) vs. benign nevus (bottom), seen on Red Green Blue (RGB) imaging, DOCI imaging, and confirmed with statistical processing via K-Means Cluster. The benign nevus demonstrates no appreciable difference in DOCI Channel 1 on the DOCI image, and therefore produces a negative result via K-means cluster on analysis.

4. DISCUSSION

This study demonstrated the promise of the DOCI device, which accurately distinguishes between melanoma and surrounding skin (in-vivo and ex-vivo), melanoma and benign nevi (in-vivo), as well as identify positive melanoma margins (ex-vivo). This multi-use device can serve as a technology that is leveraged for improving and prolonging the lives of all patients affected by melanoma, from screening in the clinic to surgical removal in the OR. Although DOCI has demonstrated utility in margin detection in mucosal head & neck malignancies in the past, this study marks the first use of DOCI in cutaneous pathologies.

Optimization of the device with appropriate filter selection must occur prior to full clinical utilization of DOCI, which was addressed in this study when comparing Channel 1 to Channel 5. Generally, the Channel 5 DOCI filter used at 530nm BPF to detect mucosal malignancy in prior studies, also demonstrated robust images in melanoma. In principle, this filter captures the tissue's autofluorescence of NADH, which is present in lower relative concentrations in tumor cells when compared to normal human tissue. However, utilizing Channel 1's LPF at 400nm produces a slightly clearer identification of melanoma vs. surrounding skin or nevus, as seen in the ROC models. The combination of both Channel 1 and Channel 5 in a predictive model in fact provides the most accurate detection of melanoma vs. surrounding skin as well as melanoma vs. nevi. The addition of the LPF is likely to account for the high autofluorescence of melanin (present in both melanoma and nevi), of which the full spectrum is then captured and accounted for in Channel 1.

This preliminary study has a small sample size with only 11 patients with melanoma included, and therefore the sensitivity and specificity may be further improved with additional patient samples. Skin and tumor surface artifact can limit DOCI imaging if scabbing, crusting, hair, and active bleeding block surface autofluorescence. Our team ensured that hair, crusting, and scabbing were gently removed, and that the area was cleaned and hemostatic to avoid this issue. Skin pigment variation remains an important challenge in skin cancer imaging techniques; the majority of the patients in this study would classify as Fitzpatrick I-IV, due to increased incidence of melanoma in this population. Looking forward, we plan to expand to other institutions and county affiliates in the next iterations of this study, actively seeking diversity, inclusivity, and equity in data collection, with optimization of DOCI to revolutionize melanoma care for all skin tones and types.

Although dermoscopy is currently used as the gold standard for screening melanotic lesions in the dermatology office, an adjunct tool providing additional confidence in need for biopsy would serve useful to expand accessibility of cutaneous melanoma screening. This is in part due to the required expertise needed for use of a dermatoscope, which is mostly utilized by board-certified dermatologists. Additionally, there is a somewhat subjective nature to this device, whereby a clinician's judgement could be variable based on their training and experience. On the other hand, the DOCI device is meant to be automated such that a technician or other non-experienced provider could produce objective results, to determine a patient's risk of melanoma quickly and reliably.

Future work will involve expansion of DOCI for melanoma in other areas of the body beyond the head and neck region, though we do not expect results to differ significantly in doing so. Work will also focus on predictive DOCI levels and markers for risk of distant metastasis and other clinical outcomes. Our team plans to also identify a wide array of cutaneous malignancies, to also include squamous cell carcinoma, basal cell carcinoma, angiosarcoma, and Merkel cell carcinoma. These cutaneous malignancies will then also be distinguished from various benign dermatologic pathologies, such as dermatofibroma and pigmented seborrheic keratosis. The DOCI device is portable, on a compact rolling cart, and is able to capture images in less than 1 minute. Modification of the device as a portable handheld could be employed for the clinic for ease of use in everyday skin screenings, and for accessibility in global health outreach programs.

Rapid margin detection in melanoma is a key area of clinical need that must be improved upon, mostly due to limited ability to undergo Mohs or frozen section analysis. While new techniques for Mohs microsurgery are emerging for melanoma, the lack of widespread use demonstrates a gap in clinical care between institutions. In this, among the cutaneous malignancies, melanoma is the most useful pathology for DOCI-guided negative resection, due to difficulty of identification on frozen section analysis. DOCI's intraoperative real-time margin detection for cutaneous melanoma could not only reduce recurrence rates and improve survival, but it would also allow for immediate reconstruction, rather than the delayed reconstruction whilst awaiting final histopathologic margins – the current gold standard. Decreasing the need for delayed reconstruction could potentially save hospital costs, in addition to lessening patient anxiety whilst waiting for the final histopathology. Further, patient quality of life can be optimized by use of DOCI for margin detection, decreasing the amount of excess tissue removed in the head and neck region during surgical resection.

A multi-purpose cutaneous malignancy device would be useful in academic centers, community hospitals, and under-resourced settings alike. In a medically underserved setting, one single device could be used in the clinic for melanoma screening, and then transported to the OR or procedure room for use in melanoma margin detection. A technician would be able to operate the machinery to aid in understaffed hospital areas, who could then relay the results to the clinician. At the same time, a clinician would be able to utilize the DOCI machine themselves for real-time feedback in providing precision surgery and superior patient care for their patients with cutaneous melanoma.

5. CONCLUSION

DOCI is a real-time imaging modality that can be utilized as a multi-purpose diagnostic and treatment device in patients with cutaneous melanoma. DOCI accurately distinguished between benign nevi and melanoma, melanoma vs. normal surrounding skin, and can detect positive margins intraoperatively. Thus, this technology has the potential to improve early detection, complete resection, quality of life, and survival outcomes for patients with melanoma.

ACKNOWLEDGEMENTS

Research reported in this publication was supported by the National Institute on Deafness and Other Communication Disorders of the National Institutes of Health under Award Number R25DC020151. The content is solely the responsibility of the authors and does not necessarily represent the official views of the National Institutes of Health.

REFERENCES

1. Siegel RL, Miller KD, Wagle NS, Jemal A. Cancer statistics, 2023. *CA Cancer J Clin*. Jan 2023;73(1):17-48. doi:10.3322/caac.21763
2. Aggarwal P, Knabel P, Fleischer AB, Jr. United States burden of melanoma and non-melanoma skin cancer from 1990 to 2019. *J Am Acad Dermatol*. Aug 2021;85(2):388-395. doi:10.1016/j.jaad.2021.03.109
3. Glazer AM, Winkelmann RR, Farberg AS, Rigel DS. Analysis of Trends in US Melanoma Incidence and Mortality. *JAMA Dermatol*. Feb 1 2017;153(2):225-226. doi:10.1001/jamadermatol.2016.4512
4. Saginala K, Barsouk A, Aluru JS, Rawla P, Barsouk A. Epidemiology of Melanoma. *Med Sci (Basel)*. Oct 20 2021;9(4)doi:10.3390/medsci9040063
5. Jethanamest D, Vila PM, Sikora AG, Morris LG. Predictors of survival in mucosal melanoma of the head and neck. *Ann Surg Oncol*. Oct 2011;18(10):2748-56. doi:10.1245/s10434-011-1685-4
6. American Academy of Dermatology Ad Hoc Task Force for the AoM, Tsao H, Olazagasti JM, et al. Early detection of melanoma: reviewing the ABCDEs. *J Am Acad Dermatol*. Apr 2015;72(4):717-23. doi:10.1016/j.jaad.2015.01.025
7. Chen SC, Bravata DM, Weil E, Olkin I. A comparison of dermatologists' and primary care physicians' accuracy in diagnosing melanoma: a systematic review. *Arch Dermatol*. Dec 2001;137(12):1627-34. doi:10.1001/archderm.137.12.1627
8. Dinnes J, Deeks JJ, Grainge MJ, et al. Visual inspection for diagnosing cutaneous melanoma in adults. *Cochrane Database Syst Rev*. Dec 4 2018;12(12):CD013194. doi:10.1002/14651858.CD013194
9. Dinnes J, Deeks JJ, Chuchu N, et al. Dermoscopy, with and without visual inspection, for diagnosing melanoma in adults. *Cochrane Database Syst Rev*. Dec 4 2018;12(12):CD011902. doi:10.1002/14651858.CD011902.pub2
10. Williams NM, Rojas KD, Reynolds JM, Kwon D, Shum-Tien J, Jaimes N. Assessment of Diagnostic Accuracy of Dermoscopic Structures and Patterns Used in Melanoma Detection: A Systematic Review and Meta-analysis. *JAMA Dermatol*. Sep 1 2021;157(9):1078-1088. doi:10.1001/jamadermatol.2021.2845
11. Pampena R, Lai M, Lombardi M, et al. Clinical and Dermoscopic Features Associated With Difficult-to-Recognize Variants of Cutaneous Melanoma: A Systematic Review. *JAMA Dermatol*. Apr 1 2020;156(4):430-439. doi:10.1001/jamadermatol.2019.4912
12. Pizzichetta MA, Stanganelli I, Bono R, et al. Dermoscopic features of difficult melanoma. *Dermatol Surg*. Jan 2007;33(1):91-9. doi:10.1111/j.1524-4725.2007.33015.x
13. Hanna S, Lo SN, Saw RP. Surgical excision margins in primary cutaneous melanoma: A systematic review and meta-analysis. *Eur J Surg Oncol*. Jul 2021;47(7):1558-1574. doi:10.1016/j.ejso.2021.02.025

14. Sahovaler A, Ziai H, Cardemil F, et al. Importance of Margins, Radiotherapy, and Systemic Therapy in Mucosal Melanoma of the Head and Neck. *Laryngoscope*. Oct 2021;131(10):2269-2276. doi:10.1002/lary.29555
15. Erickson C, Miller SJ. Treatment options in melanoma in situ: topical and radiation therapy, excision and Mohs surgery. *Int J Dermatol*. May 2010;49(5):482-91. doi:10.1111/j.1365-4632.2010.04423.x
16. Stevenson O, Ahmed I. Lentigo maligna : prognosis and treatment options. *Am J Clin Dermatol*. 2005;6(3):151-64. doi:10.2165/00128071-200506030-00002
17. Dawn ME, Dawn AG, Miller SJ. Mohs surgery for the treatment of melanoma in situ: a review. *Dermatol Surg*. Apr 2007;33(4):395-402. doi:10.1111/j.1524-4725.2007.33085.x
18. Miller CJ, Shin TM, Sobanko JF, et al. Risk factors for positive or equivocal margins after wide local excision of 1345 cutaneous melanomas. *J Am Acad Dermatol*. Aug 2017;77(2):333-340 e1. doi:10.1016/j.jaad.2017.03.025
19. Kim IA, Taylor ZD, Cheng H, et al. Dynamic Optical Contrast Imaging. *Otolaryngol Head Neck Surg*. Mar 2017;156(3):480-483. doi:10.1177/0194599816686294
20. Tajudeen BA, Taylor ZD, Garritano J, et al. Dynamic optical contrast imaging as a novel modality for rapidly distinguishing head and neck squamous cell carcinoma from surrounding normal tissue. *Cancer*. Mar 1 2017;123(5):879-886. doi:10.1002/cncr.30338
21. Huang S, Alhiyari Y, Hu Y, et al. Ex vivo hypercellular parathyroid gland differentiation using dynamic optical contrast imaging (DOCI). *Biomed Opt Express*. Feb 1 2022;13(2):549-558. doi:10.1364/BOE.443671
22. Hu Y, Han AY, Huang S, et al. A Tool to Locate Parathyroid Glands Using Dynamic Optical Contrast Imaging. *Laryngoscope*. Oct 2021;131(10):2391-2397. doi:10.1002/lary.29633
23. Cheng H, Xie Y, Pellionisz P, et al. Dynamic Optical Contrast Imaging (DOCI): System theory for rapid, wide-field, multispectral optical imaging using fluorescence lifetime contrast mechanism. *Proc Spie*. 2019;10951doi:Artn 109512t
10.1117/12.2513823

A rapid spectroscopic platform in identifying cisplatin resistance in head and neck squamous cell carcinoma

Shu-Jen Chiang^a, Po-Hang Tseng^a, Mei-Chun Lin^b, Chih-Yu Leu^c, Madhusudan Roy^a,
Chen-Yuan Dong^{*a}, Pei-Jen Lou^{*b}

^aDepartment of Physics, National Taiwan University, Taipei 106, Taiwan, R. O. C.; ^bDepartment of Otolaryngology, National Taiwan University Hospital and College of Medicine, Taipei 100, Taiwan, R. O. C.; ^cDepartment of Medical Education, National Taiwan University College of Medicine, Taipei 100, Taiwan, R. O. C.

ABSTRACT

At present, the administration of chemotherapy drugs is largely based on physician experience and clinical guidelines. Clearly, a personalized solution would significantly benefit patients in the improvement of clinical outcomes. In this work, we used a spectroscopic approach in which a water-soluble tetrazolium salt (WST-8) assay was applied to patient-derived slice organoids. WST-8 would react with intracellular dehydrogenase resulting in the formation of formazan dye. The absorption at 450 nm can be used to assess the viability of the organoids 5 days after initiation of organoid culture. With additional development, this approach may be used to improve the clinical outcome of patients undergoing chemotherapy.

Keywords: cisplatin resistance, head and neck squamous cell carcinoma, optical spectroscopy, chemotherapy

1. INTRODUCTION

The administration of chemotherapy drugs (CD) is largely based on clinical guidelines. In the case of head and neck squamous cell carcinoma, intake of tobacco products, alcohol, and viral infection are major contributing factors to the disease [1]. Frequently, HNSCC cases are detected in the advanced stages as symptoms are often absent in the early stage [2]. Treatment strategies include chemotherapy, surgery, radiotherapy, or their combination [3]. In addition, with an annual mortality of 0.35 million and a 5-year overall survival (OS) of 40-50%, HNSCC remains one of the deadliest cancers [4, 5]. Among the various treatment options, cisplatin is a common CD used [6]. However, cisplatin resistance is a major obstacle in the treatment of HNSCC patients [7]. A common practice in the clinics is to follow up with patients every three months, however, if patient response can be predicted at an earlier time point, patients should benefit from such an approach. In this study, we discuss our work on the recognition of cisplatin-resistant in patients by *in vitro* rapid drug susceptibility screening of patient tumor slice organoids (PTSO).

2. MATERIALS AND METHODS

After obtaining the HNSCC sample, it was placed into DMEM, kept on ice, and taken to the lab for analysis. The PTSOs were prepared by first embedding the sample into 4% agarose (PBS) which was prepared and stored at 65 °C. After gelling, the samples were sliced with the vibrating-blade microtome (Compressstone® VF-300, Natick, MA) at a frequency of 1 slice per 20 seconds. The thickness of each PTSO was around 150 μm. The processed PTSO was then mounted onto a 24-well culture plate and cultured with DMEM having 10% fetal bovine serum, 1% penicillin-streptomycin, and 2.5 μg/ml amphotericin B. If we needed to store the specimens for a longer period, PTSOs were frozen in a mixture of 7.5% DMSO with fetal bovine serum cooled at a rate of 1 °C/min and frozen to -80 °C.

We found that the specimens can be cultured for a period of up to 26 days. Shown in Figure 1 are sample microscopic images of the cultured PTSOs. After culturing, cisplatin of different concentrations was added to the PTSOs. Two days after

* cydong@phys.ntu.edu.tw phone: +886-02-33665196 or pjlou@ntu.edu.tw

culturing, the WST-8 assay was applied to each PTISO for determination of specimen viability. Next, cisplatin at different concentrations was added and the PTISOs were cultured for another 3 days before the next round of WST-8 assay was performed. The change in optical density in the culture media before and after cisplatin application was determined and used as an indication of drug efficacy [8]. Details of the WST-8 assay is describes as follows:

WST-8 functions by interaction with intracellular dehydrogenase. In this case, WST-8 changes to WST-8 formazan dye which absorbs strongly at 450 nm[9]. Therefore, by measuring the absorption at 450 nm viability can be assayed. To assay for WST-8, the PTISOs were grown in a media with 9.1% WST-8 for about 4 hours. At the end of the 4-hour period, the WST-8 solution was removed for optical density measurement. Next, various concentrations (0 -100 $\mu\text{g/ml}$) of cisplatin (Sigma, St. Lous, MO) were introduced to the cultivating media for 72 hours. Lastly, after 5 days of starting PTISO growth, the media having cisplatin was removed and the WST-8 assay was performed again.

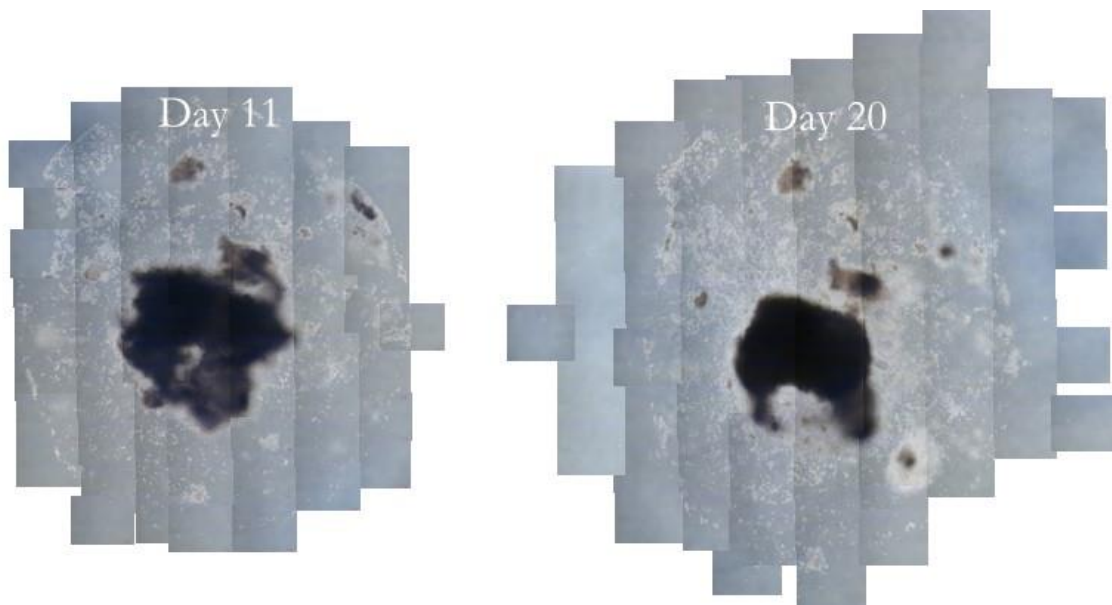


Figure 1. Long-term culturing of HNSCC PTISOs. Optical microscopy images at Days 11 and 20 show the feasibility of long-term cultivation of HNSCC PTISOs. With this specimen, we were able to culture up to Day 26 at which point, the test was terminated [8].

3. RESULTS AND DISCUSSION

Shown in Figure 2 is the relative viability of tested HNSCC PTISOs obtained at various concentrations of cisplatin for 2 patients. At each cisplatin concentration, a number of PTISOs was used. The orange bar represents change in relativity viability of a particular PTISO. The blue bar represents the average value of all the specimens tested at a given cisplatin concentration. Note that at lower concentrations of cisplatin (0 and 0.1 $\mu\text{g/ml}$), most of the specimens are viable. However, as the concentration of the cisplatin increases (10, 100 $\mu\text{g/ml}$) the specimens' viability tend to diminish.

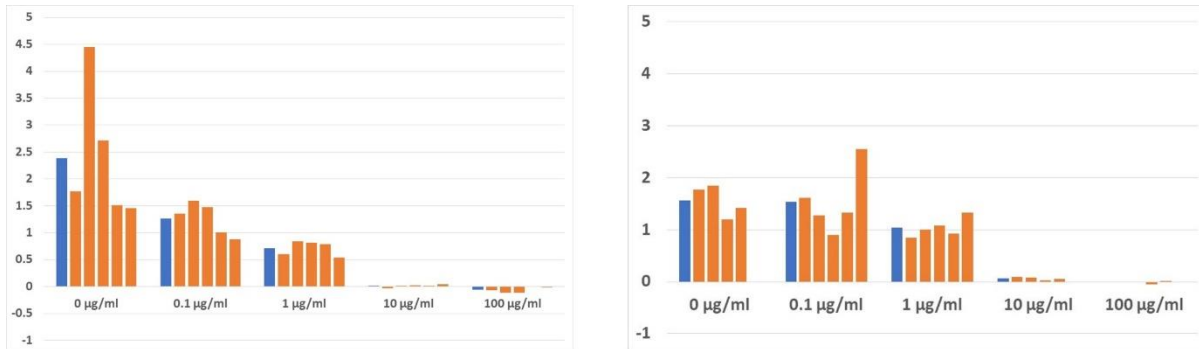


Figure 2. Comparison of relative viabilities of HNSCC PTSOs at various cisplatin concentrations. The mean value of OD change for each concentration is shown in the blue bars.

4. CONCLUSION

In this work, we evaluated the use of cisplatin resistance test for determining patient resistance to the drug. Our method calls for an initial 2-day culturing of the HNSCC PTSOs at which point the viability of the PTSOs was determined by using the WST-8 assay. Next, cisplatin at various concentrations was added to the PTSOs and the specimens were cultured for another 3 days prior to another WST-8 test. The relative change in optical densities indicated the change in PTSO viability from cisplatin application. We found that in most cases, HNSCC PTSOs decrease in viability with increasing cisplatin concentration. However, in one case, we did find a lack of sensitivity to different cisplatin concentrations, corresponding to a relatively poor survival (disease-free survival of 26 day and overall survival of 126 days.) [8]. Therefore, our approach may be used to identify patients resistant to cisplatin treatment.

5. ACKNOWLEDGMENT

This work was supported by the National Science and Technology Council (Grant 110-2112-M-002-025-MY3) of Taiwan, R. O. C.

REFERENCES

- [1] D. E. Johnson, B. Burtneß, C. R. Leemans *et al.*, “Head and neck squamous cell carcinoma,” *Nature Reviews Disease Primers*, 6(1), 92 (2020).
- [2] H. Hu, B. Li, J. Wang *et al.*, “New advances into cisplatin resistance in head and neck squamous carcinoma: Mechanisms and therapeutic aspects,” *Biomedicine & Pharmacotherapy*, 163, 114778 (2023).
- [3] J. D. Cramer, B. Burtneß, Q. T. Le, and R. L. Ferris, “The changing therapeutic landscape of head and neck cancer,” *Nature Reviews Clinical Oncology*, 16(11), 669-683 (2019).
- [4] N. Vigneswaran, and M. D. Williams, “Epidemiologic trends in head and neck cancer and aids in diagnosis,” *Oral Maxillofac Surg Clin North Am*, 26(2), 123-41 (2014).
- [5] C. Yu, Q. Li, Y. Zhang *et al.*, “Current status and perspective of tumor immunotherapy for head and neck squamous cell carcinoma,” *Front Cell Dev Biol*, 10, 941750 (2022).
- [6] V. Patil, V. Noronha, S. B. Dhumal *et al.*, “Low-cost oral metronomic chemotherapy versus intravenous cisplatin in patients with recurrent, metastatic, inoperable head and neck carcinoma: an open-label, parallel-group, non-inferiority, randomised, phase 3 trial,” *The Lancet Global Health*, 8(9), e1213-e1222 (2020).
- [7] X. Meng, Q.-Y. Lou, W.-Y. Yang *et al.*, “The role of non-coding RNAs in drug resistance of oral squamous cell carcinoma and therapeutic potential,” *Cancer Communications*, 41(10), 981-1006 (2021).
- [8] S.-J. Chiang, P.-H. Tseng, M.-C. Lin *et al.*, “In vitro assay identifying cisplatin resistance of head and neck squamous cell carcinoma,” *Oral Oncology Reports*, 7, 100053 (2023).
- [9] L. Cai, X. Qin, Z. Xu *et al.*, “Comparison of Cytotoxicity Evaluation of Anticancer Drugs between Real-Time Cell Analysis and CCK-8 Method,” *ACS Omega*, 4(7), 12036-12042 (2019).

Photobiomodulation therapy for the management of oral mucositis: a clinical case

Marcelo Saito Nogueira^{1,2,3,4,*}, Carolina Almeida Gianini^{1,6}, Raissa Biason Pereira^{1,6}, Gabriel Silvani^{1,6}, Vanderlei Salvador Bagnato^{1,4}, Vitor Hugo Panhóca^{1,4,5,6}

¹*São Carlos Institute of Physics– University of São Paulo (USP), São Carlos, São Paulo, Brazil*

²*Present affiliation: Tyndall National Institute, Cork, Ireland, Lee Maltings Complex, Dyke Parade, Cork, Ireland, Postcode: T12R5CP*

³*Present affiliation: Department of Physics, University College Cork, College Road, Cork, Ireland, Postcode: T12K8AF*

⁴*Biophotonics Laboratory, Institute of Physics of São Carlos – University of São Paulo (USP), São Carlos, São Paulo, Brazil*

⁵*Biotechnology - UFSCar, Federal University of São Carlos - UFSCar, São Carlos, São Paulo, Brazil*

⁶*Irmandade da Santa Casa de Misericórdia de São Paulo, São Paulo 01221-010, Brazil*

**Corresponding author*

E-mail address: marcelosaitonogueira@gmail.com

ABSTRACT

Oral Mucositis (OM) is an inflammatory alteration of the mucosa primarily due to the damage resulting of cytotoxic effects of radiotherapy, chemotherapy, bone marrow transplantation and stem cell transplantation. The use of photobiomodulation (PBM) therapy for oral mucositis is intended to reduce or prevent lesions from manifesting. However, there is no consensus on the treatment dosimetry based on higher treatment success rates, and no exact cause of treatment success or failure has been found for large groups of patients. Therefore, optimizing treatment protocols and investigating causes affecting treatment outcomes is of paramount importance to decrease pain, hospitalization time, death rates of oncological patients while giving them improved quality of life via nutrition without pain. This case study shows a successful example of the treatment outcome of a new PBM therapy protocol for OM where we concluded that PBM therapy can be used as a potentially effective preventive and curative treatment of OM.

Keywords: Oral mucositis, Low-Level Laser Therapy, Photobiomodulation, Phototherapy, LLLT, Chemotherapy, Head and neck surgery, Radiotherapy, Odontology

1. INTRODUCTION

Oral Mucositis (OM) is an inflammatory alteration of the mucosa primarily due to the damage resulting of cytotoxic effects of radiotherapy, chemotherapy, bone marrow transplantation and stem cell transplantation. In certain cases, such damage, therapeutic adverse effects, and pain caused by mucositis do not allow patients to chew, swallow and go through conventional OM treatment (e.g., local anaesthetics and antifungal tablets or drops)¹. In these cases, alternatives such as external application of photobiomodulation (PBM) therapy or Low-Level Laser Therapy (LLLT) are effective.

The use of PBM therapy for OM is intended to reduce or prevent lesions from manifesting²⁻⁴, as well as decrease the pain sensitivity in oral mucosa⁵. In general, recommended parameters for the management of OM in head and neck cancer patients undergoing chemoradiation include power output between 10 and 150 mW, energy density of 2–5 J/cm², and wavelengths from 633–685 nm and/or 780–830 nm⁶. Also, pain relief typically involve the same parameters, but with energy density of 10–15 J/cm². In cases of external light application, the use of red (380nm - 700nm) and infrared (700nm

- 1070nm) wavelengths enable large penetration depth in soft and hard tissues⁷⁻²⁷, making it easier for light to reach OM lesions.

However, there is no consensus on the treatment dosimetry based on higher treatment success rates, and no exact cause of treatment success or failure has been found for large groups of patients. Therefore, optimizing treatment protocols and investigating causes affecting treatment outcomes is of paramount importance to decrease pain, hospitalization time, death rates of oncological patients while giving them improved quality of life via nutrition without pain.

This case study shows a successful example of the treatment outcome of a new PBM therapy protocol for OM by using punctual and area applications of red (680 nm) and infrared (808 nm) lasers over lesion areas and mucous membranes. Both punctual and area applications involved 3J per irradiated location over 30 seconds.

2. CASE REPORT

In 3 June 2023, the patient MC, 89 years old, Caucasian, phototype 2, had a malignant tumor located between the nose and the roof of the mouth. He was undergoing radiotherapy and developed mucositis. The patient provided his informed consent by signing the Informed Consent Form for treatment and was evaluated by a dentist at the Photodynamic Therapy Unit of the Santa Casa de Misericórdia de São Carlos–SP. Additionally, they received oral hygiene instructions, including dental brushing after meals, daily flossing, and rinsing with a 10 ml solution containing 1.5 mg of benzydamine hydrochloride, ethyl alcohol, mint flavor, glycerol, methylparaben, polysorbate, sodium saccharin dihydrate, and purified water (twice daily).

The clinical evaluation involved assessing the OM severity OM based on the World Health Organization (WHO) classification, which considers the following criteria²⁸:

Grade 0 - absence of signs and symptoms;

Grade 1 - presence of erythema with no lesions;

Grade 2 - ulcerated mucosa, but the patient can still eat normally;

Grade 3 - presence of ulcers, intense pain, and the patient can only consume liquids;

Grade 4 - the patient requires parenteral nutrition and continuous analgesic support.

The patient's OM lesion (>1.5 cm) was categorized as Grade 3. Due to the location of the OM lesion, the patient had difficulties to eat, leading to worsening of his already compromised immune system as a side effect of radiotherapy. Since his immune system was weak, he also had a labial Herpes lesion type 1 in his nose. We performed the post-treatment follow up 15 days after the last treatment session (i.e., at day 30).

3. MATERIALS AND METHODS

The treatment protocol was developed based on parameters of previous protocols for the treatment devices used in this study^{29,30}. We used LLLT three times a week (Monday, Wednesday and Friday), the Recover® device (MMOptics, São Carlos, SP, Brazil) was applied on each OM lesion for 30 seconds to deliver 3J (total energy) in each application. Recover® emits light infrared wavelength (808nm) with 100 mW of laser power. After Recover® application, Vacumlaser® (MMOptics, São Carlos, SP, Brazil) illumination was applied over the area of OM lesions for 30 seconds and on the internal cheek mucosa, as well as the mucosa of both dorsal and lateral surfaces of tongue. The Vacumlaser illumination used 680 nm and 808 laser wavelengths, total energy delivered was 3J. If no lesion was present in the entire area, PBM was applied to prevent lesions from arising. In this patient, preventive PBM was performed in the inferior lip and cheeks. Since the mouth movement of the patient was restricted, we applied Vacumlaser® illumination on patient cheeks externally.

4. RESULTS AND DISCUSSION

Over the period of 30 days (in 3 July 2023), the OM lesion grade decreased from grade 3 to grade zero (complete recovery). The grade continued to be grade zero after 15 days (post-treatment follow up). The patient's labial herpes lesion type 1 was also completely healed after 30 days of treatment. Based on the treatment outcome, LLLT successfully

controlled lesions that appear in the oral cavity of a patient with head and neck cancer, in addition to improving their quality of life. Low-power laser therapy has been shown to be effective in managing OM in many studies, minimizing lesions and the time they remain in the oral cavity, resulting in the healing process being achieved as well. Furthermore, this laser therapy relieves painful symptoms. It is important to note that the application LLLT in oncological patients should take into consideration the rise of nitric oxide (NO), which can increase the blood supply of tumors (intrinsically highly vascularized).

5. CONCLUSIONS

We concluded that PBM therapy can be used as a complementary therapy and potentially effective preventive and curative treatment of OM.

ACKNOWLEDGEMENTS

Marcelo Saito Nogueira received his salary from Science Foundation Ireland (SFI): grant ID SFI/15/RP/2828 and 22/RP-2TF/10293.

REFERENCES

- [1] Neville, B., [Patologia oral e maxilofacial], Elsevier Brasil (2011).
- [2] Hafner, D., Hrast, P., Tomaževič, T., Jazbec, J. and Kavčič, M., “Photobiomodulation for Chemotherapy-Induced Oral Mucositis in Pediatric Patients,” *Biomolecules* **13**(3), 418 (2023).
- [3] Figueiredo, A. L. P., Lins, L., Cattony, A. C. and Falcão, A. F. P., “Laser terapia no controle da mucosite oral: um estudo de metanálise,” *Rev. Assoc. Med. Bras.* **59**(5), 467–474 (2013).
- [4] Araújo, B. A., Barros, J. N., Junior, H. C. F., Gottardo, V. D., Salmeron, S. and Mariano, J. R., “O impacto da laserterapia na mucosite oral,” *Rev. Uningá* **55**(S3), 39–46 (2018).
- [5] Panhoca, V. H., Sene-Fiorese, M., Tamae, P. E., Paolillo, F. R. and Bagnato, V. S., “Clinical Treatment with Photobiomodulation Combined with Vacuum Therapy in Temporomandibular Disorders,” *Int. J. Health Sci. (Qassim)*. **11**(2), 25–31 (2023).
- [6] Kalhori, K. A. M., Vahdatinia, F., Jamalpour, M. R., Vescovi, P., Fornaini, C., Merigo, E. and Fekrazad, R., “Photobiomodulation in oral medicine,” *Photobiomodulation, Photomedicine, Laser Surg.* **37**(12), 837–861 (2019).
- [7] Nogueira, M. S., Raju, M., Gunther, J., Grygoryev, K., Komolibus, K., Lu, H. and Andersson-Engels, S., “Diffuse reflectance spectroscopy for determination of optical properties and chromophore concentrations of mice internal organs in the range of 350 nm to 1860 nm,” *Proc. SPIE 10685 Biophotonics Photonic Solut. Better Heal. Care VI* **10685**, 106853G (2018).
- [8] Nogueira, M. S. and Guimarães, F. E. G., “Photophysical processes on biological tissues and photodynamic therapy using steady-state and time-resolved fluorescence techniques: diagnosis applications, dosimetry and photodegradation kinetics,” *Livro de Resumos* (2016).
- [9] Panhóca, V. H., Nogueira, M. S. and Bagnato, V. S., “Treatment of facial nerve palsies with laser and endermotherapy: a report of two cases,” *Laser Phys. Lett.* **18**(1), 15601 (2020).
- [10] Panhóca, V. H., Nogueira, M. S. and Bagnato, V. S., “Laser and vacuum therapy for treatment of facial nerve palsies,” *Imaging, Ther. Adv. Technol. Head Neck Surg. Otolaryngol.* **2022** **11935**, 39–48 (2022).
- [11] Nogueira, M. S., Maryam, S., Amissah, M., Lu, H., Lynch, N., Killeen, S., O’Riordain, M. and Andersson-Engels, S., “Evaluation of wavelength ranges and tissue depth probed by diffuse reflectance spectroscopy for colorectal cancer detection,” *Sci. Rep.* **11**(1), 1–17 (2021).
- [12] Nogueira, M. S., Maryam, S., Amissah, M., Lynch, N., Killeen, S., O’Riordain, M. and Andersson-Engels, S., “Benefit of extending near-infrared wavelength range of diffuse reflectance spectroscopy for colorectal cancer detection using machine learning,” *Eur. Conf. Biomed. Opt.*, EW4A--16 (2021).
- [13] Nogueira, M. S., Raju, M., Gunther, J., Maryam, S., Amissah, M., Killeen, S., O’Riordain, M. and Andersson-Engels, S., “Optical determination of superficial and deeper tissue biochemistry and microstructure for delineation and early detection of colorectal cancer,” *Eur. Conf. Biomed. Opt.*, ETu3A--1 (2021).

- [14] Nogueira, M. S., Raju, M., Komolibus, K., Grygoryev, K. and Andersson-Engels, S., "Assessment of tissue biochemical and optical scattering changes due to hypothermic organ preservation: a preliminary study in mouse organs," *J. Phys. D. Appl. Phys.* **54**(37), 374003 (2021).
- [15] Nogueira, M. S., Raju, M., Gunther, J., Maryam, S., Amissah, M., Lu, H., Killeen, S., O'Riordain, M. and Andersson-Engels, S., "Tissue biomolecular and microstructure profiles in optical colorectal cancer delineation," *J. Phys. D. Appl. Phys.* **54**(45), 454002 (2021).
- [16] Saito Nogueira, M., Maryam, S., Amissah, M., McGuire, A., Spillane, C., Killeen, S., Andersson-Engels, S. and O'Riordain, M., "Insights into Biochemical Sources and Diffuse Reflectance Spectral Features for Colorectal Cancer Detection and Localization," *Cancers (Basel)*. **14**(22), 5715 (2022).
- [17] Bomfin, L. S., Kitakawa, D., Nogueira, M. S., e Silva, L. F. das C. and others., "Low Level Laser Therapy as adjuvant treatment for lower lip lesion," *Lat. Am. Opt. Photonics Conf.*, M2B--6 (2022).
- [18] Mousavi, M., Moriyama, L. T. T., Grecco, C., Nogueira, M. S., Svanberg, K., Kurachi, C. and Andersson-Engels, S., "Photodynamic therapy dosimetry using multiexcitation multiemission wavelength: toward real-time prediction of treatment outcome," *J. Biomed. Opt.* **25**(6), 63812 (2020).
- [19] de Andrade, C. T., Nogueira, M. S., Kanick, S. C., Marra, K., Gunn, J., Andreozzi, J., Samkoe, K. S., Kurachi, C. and Pogue, B. W., "Optical spectroscopy of radiotherapy and photodynamic therapy responses in normal rat skin shows vascular breakdown products," *Proc. SPIE 9694 Opt. Methods Tumor Treat. Detect. Mech. Tech. Photodyn. Ther.* **XXV 9694**, 969410 (2016).
- [20] Nogueira, M. S., Jayet, B., Matias, J. S., Gunther, J. E., Tyndall, C. and Andersson-Engels, S., "Biophotonics web application for computer simulations in diffuse optics: fostering multidisciplinary education and research," *Proc. SPIE 11958, Photonics West*, 11958-18 (2022).
- [21] Salvio, A. G., Ramirez, D. P., Inada, N. M., Stringasci, M. D., Nogueira, M. S. and Bagnato, V. S., "Fractionated illumination in a single visit photodynamic therapy for basal cell carcinoma," *B. Abstr.* (2017).
- [22] Salvio, A. G., Ramirez, D. P., Nogueira, M. S., Stringasci, M. D., Oliveira, E. R., Inada, N. M. and Bagnato, V. S., "Evaluation of pain and treatment effect during large area photodynamic therapy in 140 patients with widespread actinic keratosis of upper limbs," *B. Abstr.* (2017).
- [23] Nogueira, M. S., Lacerenza, M., Sekar, S. K. V., Buttafava, M., Pifferi, A., Tosi, A., Contini, D. and Andersson-Engels, S., "Broadband extraction of tissue optical properties using a portable hybrid time-resolved continuous wave instrumentation: characterization of ex vivo organs," *Clin. Transl. Biophotonics*, TM2B--3 (2020).
- [24] Marcelo, S. N., "Biophotonics for pandemic control: large-area infection monitoring and microbial inactivation of COVID-19," *Photodiagnosis Photodyn. Ther.* (2020).
- [25] Nogueira, M. S., "Optical theranostics and treatment dosimetry for COVID-19 lung complications: towards increasing the survival rate of vulnerable populations," *Photodiagnosis Photodyn. Ther.* (2020).
- [26] Nogueira, M. S., "Biophotonic telemedicine for disease diagnosis and monitoring during pandemics: overcoming COVID-19 and shaping the future of healthcare," *Photodiagnosis Photodyn. Ther.* (2020).
- [27] e Silva, L. F. das C. and de Carvalho, M. S. N., "Optical techniques for fast screening--towards prevention of the coronavirus COVID-19 outbreak," *Photodiagnosis Photodyn. Ther.* (2020).
- [28] Albuquerque, K. B. de., "Laserterapia de baixa potência em mucosite oral." (2019).
- [29] Ferreira, L. T., Souza, V. B., Ferreira, S. A., Simão, G., Aquino Jr, A. E., Nogueira, M. S., Bagnato, V. S. and Panhóca, V. H., "Application of low-level laser therapy in trigeminal neuralgia: a clinical case," *Imaging, Ther. Adv. Technol. Head Neck Surg. Otolaryngol.* **2023 12354**, 12-17 (2023).
- [30] Panhóca, V. H., Aquino Junior, A. E., Souza, V. B., Ferreira, S. A., Ferreira, L. T., Souza, K. J. O., Tamae, P. E., Saito Nogueira, M. and Bagnato, V. S., "Effects of red and infrared laser therapy in patients with tinnitus: a double-blind, clinical, randomized controlled study combining light with ultrasound, drugs and vacuum therapy," *J. Pers. Med.* (2023).

Intraoral scanner and stereographic 3D print in prosthodontics: three-year evaluation of *in vitro* and *in vivo* approaches

Tatjana Dostalova^{a*}, Adam Nocar^a, Hana Eliasova^a, Milan Macek^b, Petra Hliňáková^a, Aleš Procházka^c

^a Department of Stomatology, Charles University 2nd Faculty of Medicine and Motol University Hospital, Prague, V Uvalu 84, 150 06, Prague, Czech Republic
E-mail: tatjana.dostalova@fnmotol.cz; Tel. +420 224 433 101; Fax: +420 224 433 120

^b Department of Biology and Medical Genetics, Charles University 2nd Faculty of Medicine and Motol University Hospital, Prague, V Uvalu 84, 150 06, Prague, Czech Republic

^c Department of Computing and Control Engineering, University of Chemistry and Technology in Prague, 166 28 Prague, Czech Republic

ABSTRACT

In prosthodontics, 3D printing primarily relies on intraoral scanners equipped with a handheld camera, computer, and software. These scanners capture and reconstruct the three-dimensional geometry of the dental arch. Traditional plaster models of teeth are typically obtained through an impression process, where the choice of appropriate impression material is determined by the desired model type. Subsequently, the dental impression is covered with plaster in the laboratory. Three-dimensional (3D) printing, formerly an industrial technology with a development history spanning over forty years, is based on creating a 3D model of any shape from a digitally prepared scan, employing an addition of selected material. The thickness of the layers in the printing process depends on the technology of the used printer and the quality of the print. The layers are systematically applied, and cured, and, after this process, a complete model is generated. 3D printing can be utilized to prepare models for various applications, including prosthodontics, orthodontics, surgery, and more. Our study aimed to assess stereolithography-printed models *in vitro* and *in vivo* over the last three years.

Keywords: laser in medicine, diode laser, dentistry, orthodontics, intraoral scanner 3Shape TRIOS, stereolithography Printer Formlabs 2

1. INTRODUCTION

The traditional methods for obtaining standard plaster models of teeth and dental arches involve an impression process, where suitable impression material is selected and plaster is used to create casts in the laboratory. Intraoral dental arch impressions are conventionally employed to document dental anatomy, alveolar bone, mucosa, and gingival shape in various fields such as prosthetics, orthodontics, or implantology^{1,2}. However, drawbacks of these classical methods include patients experiencing discomfort during the impression process and/or issues such as undesirable bubble formation in the material. Plaster models are prone to easy destruction, and their reusability is challenging. Moreover, storing these models demands significant storage requirements. However, there is the potential for recycling of the plaster material.

An emerging technique for precise dental arch reconstruction is represented by dental arch digitalisation. In this respect, 3D printing is a key aspect of this approach, involving the creation of a 3D model of any shape from the selected material based on a digitally prepared scan. The layer thickness within the 3D printing process depends on the printer technology and print quality. The layers are gradually applied, cured, and, at the end of the process, result in a complete model. Hence the 3D printing method generates appropriate models for various dental applications, including prosthodontics, orthodontics, and orofacial surgery³.

In contrast to traditional methods, 3D scanners play a crucial role in capturing and reconstructing the three-dimensional geometry of dental arches using video cameras, computers, and specialized software^{4,5}. A comparative analysis of ten intraoral scanners developed between 2015 and 2020 had been performed, using a specially printed SLS dental model with reference points. Amornvit et al.⁴ evaluated e.g. the Scanners Trios 3 (normal and high-resolution mode), Trios 4 (normal

and high-resolution mode) (3Shape Trios A/S, Copenhagen, Denmark), iTero Element, iTero 2, and iTero 5D Element (Align Technologies, San Jose, California, USA), Dental Wings (Dental Wings, Montreal QC, Canada), Panda 2 (Pentum Technologies, Shanghai, China), and Medit i500 (Medit Corp., Seoul, South Korea) systems. The devices evaluated in the experiment, namely Planmeca Emerald™ (Planmeca, Helsinki, Finland) and Aoralscan (Shining 3D Tech. Co., Ltd., Hangzhou, China), demonstrated similar precision, confirming their suitability for clinical practice. Among the scanners assessed, Trio's series exhibited the most favourable scan results.

The term stereolithography (SLA), patented by Chuck Hull in 1984 (U.S. patent No. 4575330), involves the layer-by-layer laser beam curing of photosensitive polymers. This process, based on digital scans, repetitively polymerizes resin layers to create a 3D model of the dental arch. The precision of SLA printing in dentistry ranges from 25 to 100 µm, directly tied to the number of layers. The resulting layer thickness depends on the printer technology and print quality^{6,7,8}.

The 3D printing technology produces models for prosthodontics, orthodontics, surgery, and clinical applications such as 3D guides or splints for implants and maxillofacial surgery. CAD/CAM technologies facilitate the production of special copings and frameworks for implant and dental restorations. Various materials, including polymers, composites, ceramics, and metal alloys, are utilized. The 3D SLA print, compared to a gypsum model, offers far greater accuracy⁹. A previous study⁸ utilizing scanning electron microscopy revealed that plaster models exhibited a grainy surface structure with sharp edges of orthorhombic crystals, while SLA surfaces were more homogeneous and smoother, with only residual layering polymer visible. The significance lies not only in the measurements of the models but also in their surface quality.

The main objective of our study was to evaluate stereolithography-printed models both *in vitro* and *in vivo* within three years of their utilisation in selected cases of rare diseases.

2. MATERIALS AND METHODS

Subjects and intraoral scanning

Another advantageous aspect of the utilised device is its integration into the Motol University Hospital computer network, enabling direct connectivity between the 3D printer facility and respective dental laboratories. This “direct” network-based connection allows the utilization of CAD/CAM technology for crafting crowns, bridges, and implants (CAD - computer-aided design for the computer-based design of future prosthetic work / CAM - computer-aided manufacturing for the computer-supported milling of crowns and bridges). This not only facilitates precise manufacturing but also allows for the measurement and long-term monitoring of models, providing insights into the patient's growth and treatment progress.

Treated cases with various rare diseases

The cohort under investigation comprises eleven children and young adolescents diagnosed with rare head and neck disorders as per their Orpha.net/OMIM.org designation. These individuals received treatment through interdisciplinary collaboration, benefiting from the expertise of a multidisciplinary therapy team aimed at minimizing therapy-related risks and optimising post-treatment outcomes. All affected patients experienced discomfort during standard impressions due to their underlying conditions, facial dysmorphism or associated various degrees of intellectual disability. Another compounding problem was associated with bubble formation in the impression material due to the common patient's non-adherence with the dental impression process.

Effective communication is maintained by the EU (e.g. within the ERN Cranio network- <https://www.ern-cranio.eu/>) and domestic coordinators among individual specialists (e.g. medical genetics, otorhinolaryngology), patients, and their families. Dentists, orthodontists, prosthodontists, implantologists, and maxillofacial surgeons collaborate in multidisciplinary teams to offer the optimal combination of treatments. The team coordinator oversees all administrative aspects of the team, including database management and research supervision.

Patients diagnosed with Amelogenesis imperfecta (OPRHA: 88661), Ellis-Van Creveld syndrome (ORPHA: 289), various types of ectodermal dysplasia (ORPHA: 3253), and Kabuki syndrome (OPRHA: 2322) underwent thorough examination, genomic testing (data available upon request) and received multidisciplinary therapy. The foundation of this approach, however, lies in the complex clinical and molecular genetics of rare diseases. Through the use of Trios® 3Shape, we

established streamlined cooperation with our patients, providing fast, easy, and accurate 3D real-colour impressions of the upper and lower jaw, including bite registration. Additionally, specialized software was employed for measuring distances, angles, and planes. The 3D print serves as the foundation for medical documentation and can be utilized for dental and orthodontic analyses and therapies, such as composite veneers, NuSmile crowns, removable children's dentures, and removable orthodontic appliances, among others.



Figure 1: Photos of patient's teeth; standard impressions and plaster cast models; intraoral digitals scans and models including virtual articulation; SLA 3D printer; CAD/CAM technology – crowns, bridges, implants reconstructions.

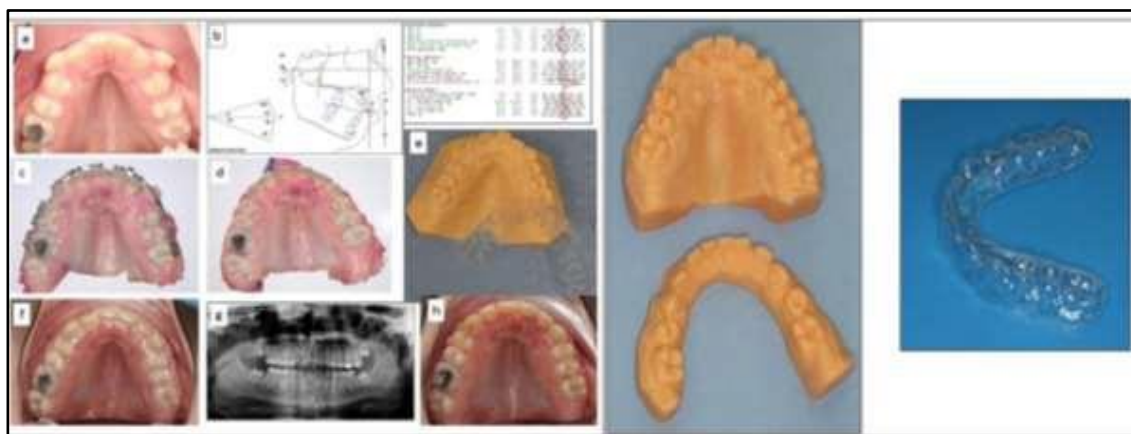


Figure 2: 13-year-old boy with compression in upper dental arch was able to use fixed dental appliance; photos before and after therapy; 3D intraoral scans before and after therapy from ERN CRANIO database. 2nd part of database are the 3D dental models + 3D print after 3 years + removable retainer.

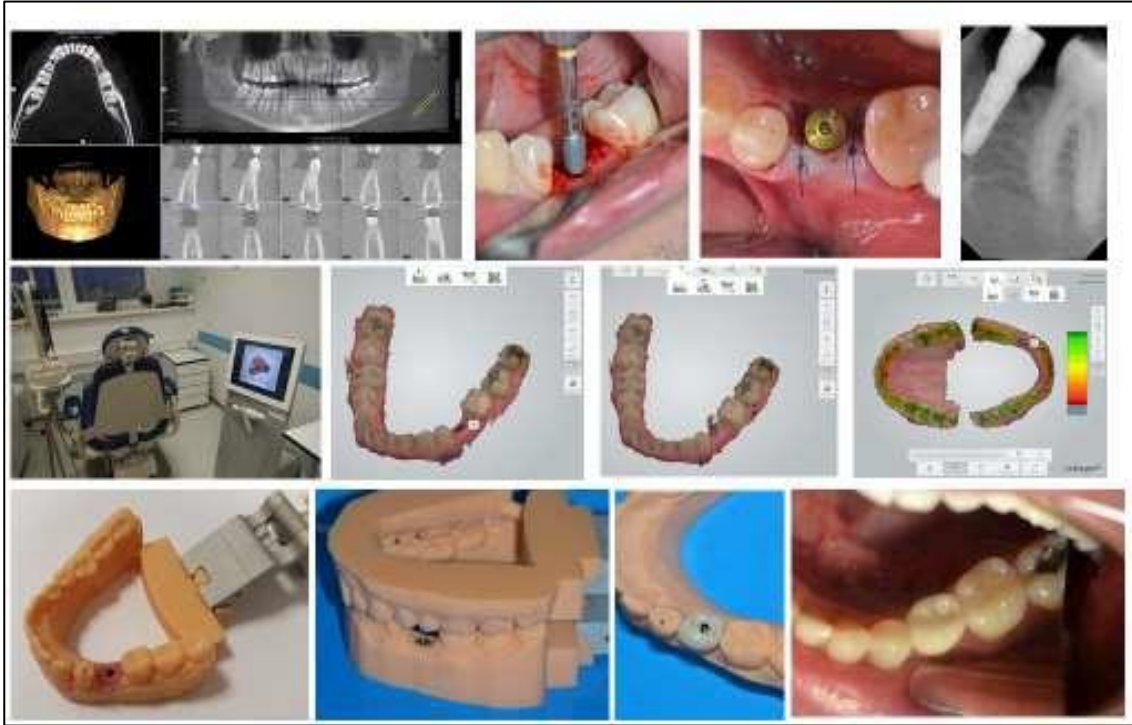


Figure 3: Patient with anodontia 35: CBCT X-ray image analysis, following implant Astra EV insertion and after implant osseointegration, crown was prepared using scanner, 3D print – STL models of upper and lower dental arch; the patient after therapy.



Figure 4: Upper and lower dental arch scan + SLC models of upper and lower dental arch following CAD/CAM ridges preparation from Zirkon framework – 5 years after reconstruction.



Figure 5: Patient with implants; 3D SLA reconstruction including KAVO virtual articulation. Implant osseointegration after 5 years.



Figure 6: Patient with CAD/CAM - ATLANTIS™ Abutment; intraoral scan and virtual model.

3. RESULTS AND DISCUSSION

Implementing 3D scanning and printing in stomatology, involving dental and oral health, can greatly enhance treatment planning, patient education, and the creation of dental appliances. We implemented this technology in several ways including (see also illustrative Figures 1-6):

- the determination of the use of the 3D technology in practice (e.g.-for creating dental models, orthodontic appliances, implants) and aims to achieve, like improved accuracy, patient comfort, or reduced treatment time;
- the choice of the right equipment as intraoral scanners that are compatible with treatment needs and dental 3D printers based on the materials which support and the precision that offer;
- the use of appropriate mathematical software tailored for dental applications to design and modify dental models;
- the integration of 3D technology into the existing workflows.

Specific research *in vitro* included a comparison of plaster cast and virtual models^{1, 2, 11, 12, 13}, mathematical modelling of the lower and upper jaw to have the possibility to find changes of their parameters during the therapy as presented in Figures 7 and 8, augmented reality use for comparison of real and simulated structures¹⁴ and the implementation of general signal processing methods in the dental research². Detail methods, results, general signal processing methods, and further references are in relevant references^{15, 16}.

Based on the aforementioned steps, we integrated 3D scanning and printing into the therapy of University Hospital Motol - Department of Stomatology to enhance treatment outcomes and patient satisfaction. The new therapeutic system was the most effective mainly for uncooperative patients e.g. small children, patients with rare diseases (Figure 2), patients with anodontia (Figure 3), patients where scans upper and lower dental arch + SLC models of upper and lower dental arch in virtual articulator KAVO and CAD/CAM crown and bridges from Zirkon framework are necessary (Figure 4). Following group contained patients with implants and virtual articulation KAVO process reconstruction (Figure 5). Six healthy patients were also treated with CAD/CAM - ATLANTIS™ Abutment, where were prepared scans and reconstruction with virtual model only (Figure 6).

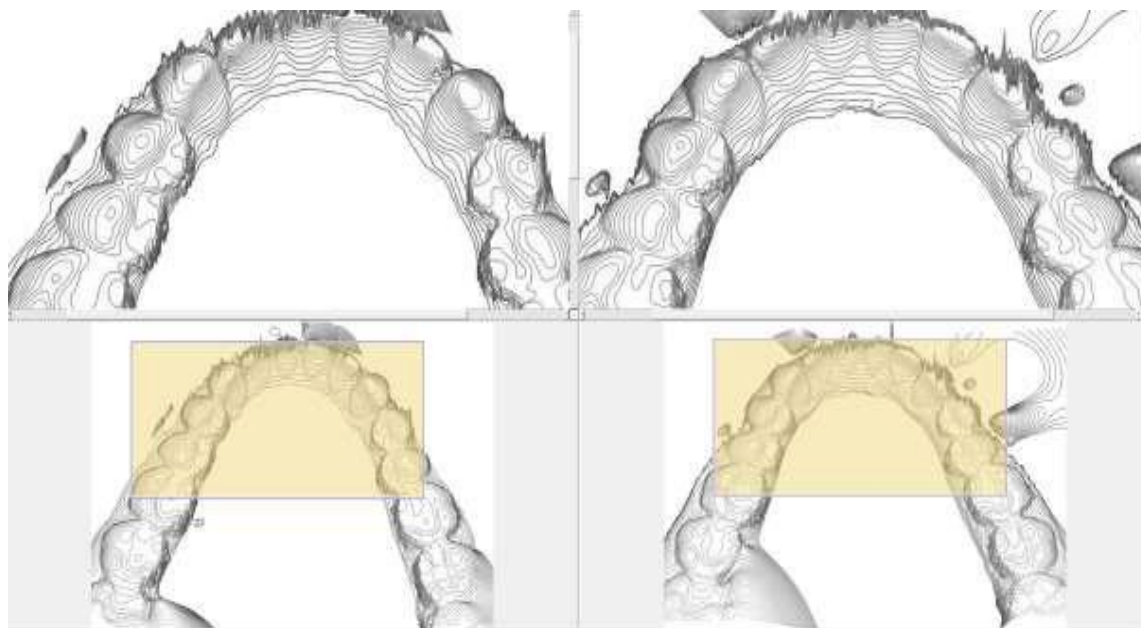


Figure 7: Registration of 3D dental models with selected fixed points.

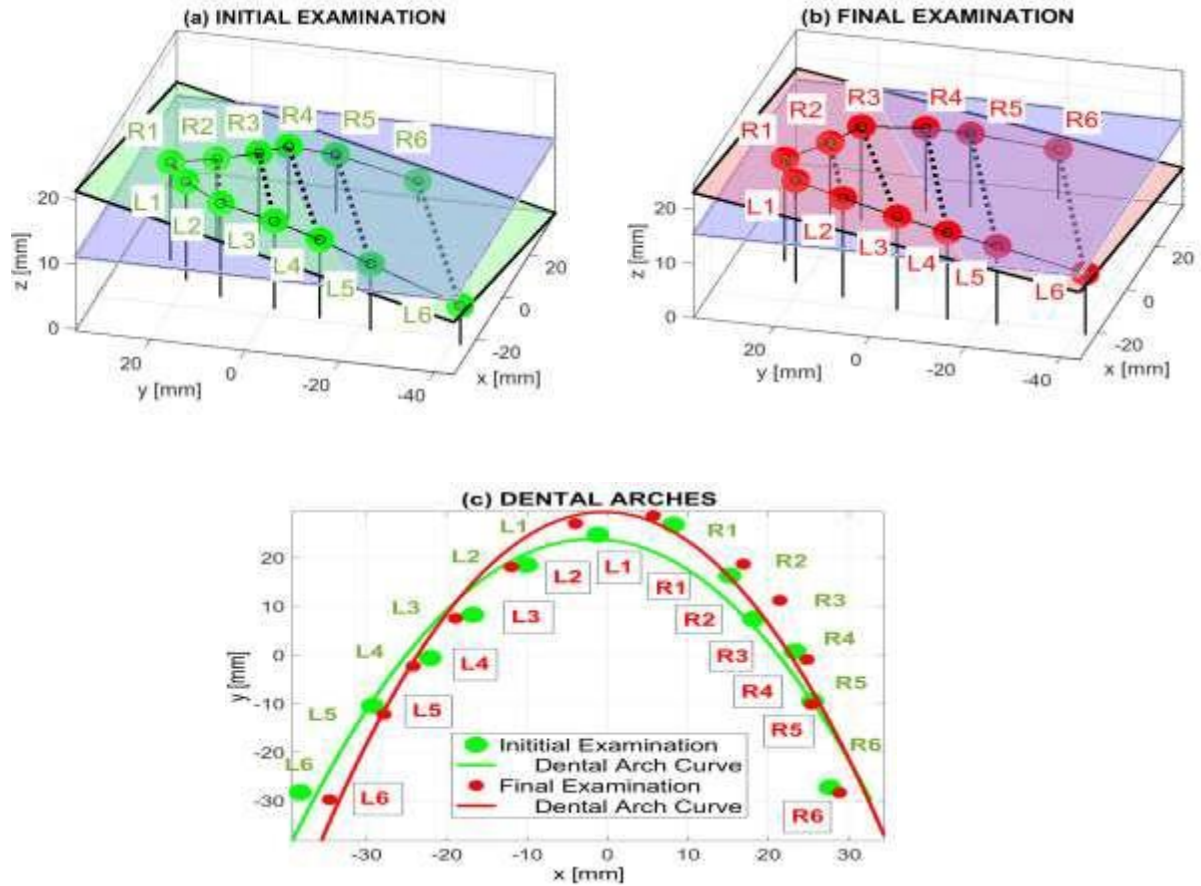


Figure 8: The spatial location of teeth centers detected by the two-camera system and used for evaluation of the corresponding teeth distances, together with their dental planes before and after rotation into the horizontal position for examination (a) before the treatment, (b) after the treatment, and (c) for the location of teeth centers rotated to the horizontal plane and the dental arch evaluated by the mean square method.

4. CONCLUSION

Our study aimed to evaluate stereolithography printed models *in vitro* and *in vivo* within 3 years of their utilisation at our department. Digitization of dental models significantly changes established dental procedures. Digitization can be divided into direct and indirect approaches. Direct digitization means the acquisition of data on the oral cavity without the use of standard impression materials and model materials. Indirect digitization means the scanning of dental impressions or plaster models.

Indirect digitization of dental models has long been used in dental laboratories, but direct digitization is a relatively new approach that allows us to completely avoid the classic process of impression of the patient's mouth. With advancing improvement, clinical protocols are being accelerated and simplified, where intraoral scanning does not take longer than conventional impression technique, but the data distribution to the laboratory and subsequent object design with the production of the desired product can be significantly faster.

We confirmed that intraoral scanning and the process of digitalization can prepare precise models, including articulation with the simulation of contactless articulation movements without the unpleasant feelings that are associated with the classic impression process and model preparation. The 3D object is created from individual layers of material where objects have complex geometry, where plastics, ceramics and metals can be used in the production of individualized objects, such as denture models, navigation implant logical templates, prosthetic metal structures or temporary crowns. The system can prepare 3D archives and 3D treatment plans including 3D measurements.

Of great importance, there are not only models' measures but also their surface quality. The evaluation of stereolithography printed models in vitro and in vivo after 3 years confirmed that clinical reconstructions were clinically stable and also precise in the roentgenological images. Finally, our study provided additional line of positive evidence for the clinical use of 3D intraoral scanning in clinical stomatology.

ACKNOWLEDGEMENT

This research has been supported by project No. 00064203 (FN MOTOL) and by Iceland, Liechtenstein a Norway via EHP funds reg. n.: ZD-ZDOVA2-001. We would like to thank participating families in this study.

Ethics approval

The study was approved by the relevant Institutional Review Boards of General University Hospital in Prague (reference no. 65/16) and Motol University Hospital (ref. no. EK-973IGA 1.12/11). The research followed the provisions of Art. 28-29 of the Act 373/2011 Coll., and was in line with the World Medical Association the "Declaration of Helsinki" principles. Patients or their legal guardians and available unaffected first-degree relatives signed informed consent before taking part in the study.

Conflict of interest statement

The authors have no conflict of interest that could influence the content or processing of this manuscript.

Consent to publish Additional informed consent was obtained from all individual participants for whom identifying information is included in this article.

REFERENCES

- [1] Kasparova, M., Grafova, L., Dvorak, P., Dostalova T., Prochazka A., Eliasova H., Prusa J., Kakawand S.: **Possibility of reconstruction of dental plaster cast from 3D digital study models.** BioMedical Engineering OnLine (2013), 12:49, pp. 1-11, DOI: 10.1186/1475-925X-12-49.
- [2] Eliasova, H., Dostalova, T., Jelinek, M., Remsa, J., Bradna, P., Prochazka, A., Kloubcova, M.: **Surface morphology of three-dimensionally printed replicas of upper dental arches.** Applied Sciences (Switzerland), (2020), 10 (16), art. no. 5708, DOI: 10.3390/app10165708.
- [3] Khorsandi, D., Fahimipour, A., Abasian, P., Saber, S.S., Seyedi, M., Ghanavati, S., Ahmad, A., De Stephanis, A.A., Taghavinezhaddilami, F., Leonova, A., Mohammadinejad, R., Shabani, M., Mazzolai, B., Mattoli, V., Tay, FR., Makvandi P.: **3D and 4D printing in dentistry and maxillofacial surgery: printing techniques, materials, and applications.** Acta Biomater (2021), 122 (1), pp. 26-49. DOI: 10.1016/j.actbio.2020.12.044.
- [4] Amornvit, P., Rokaya, D., Sanohkan, S.: **Comparison of accuracy of current ten intraoral scanners.** Biomed Res Int. (2021), art. no. 2673040, DOI: 10.1155/2021/2673040.
- [5] Richert, R., Goujat, A., Venet, L., Viguie, G., Viennot, S., Robinson, P., Farges, J.Ch., Fages, M., Ducret, M.: **Intraoral scanner technologies: a review to make a successful impression.** J Healthc Eng. 2017; 2017: 8427595, DOI: 10.1155/2017/8427595.
- [6] Formlabs.com. Professional 3D Printing Materials for Digital Dentistry | Formlabs. <https://dental.formlabs.com/> (2021).
- [7] <https://www.stratasys.com/materials/search/biocompatible> (2021).
- [8] Dostalova, T., Kasparova, M., Kriz, P., Halamova, S., Jelinek, M.B., Bradna, P., Mendricky, R.: **Intraoral scanner and stereographic 3D print in dentistry - quality and accuracy of model - new laser application in clinical practice.** Laser Physics. (2018), 28, Article ID 125602.

- [9] Nulty A.: **A comparison of trueness and precision of 12 3D printers used in dentistry.** BDJ Open. (2022), 8(1): 14, DOI: 10.1038/s41405-022-00108-6.
- [10] Marti Marti, B., Sauret-Jackson, V., Darwood A.: **3D printing in dentistry.** Br Dent J. (2015), 219, pp. 521-529, DOI:10.1038/sj.bdj.2015.914
- [11] Ender, A., Attin, T., Mehl A.: **In vivo precision of conventional and digital methods of obtaining complete-arch dental impressions.** J Prosthet Dent. (2016) 115, pp. 313-320, DOI: 10.1016/j.prosdent.2015.09.011.
- [12] Winkler, J., Gkantidis, N.: **Trueness and precision of intraoral scanners in the maxillary dental arch: an in vivo analysis.** Sci Rep. (2020), 10(1), 1172, DOI: 10.1038/s41598-020-58075-7.
- [13] Etemad-Shahidi, Y., Qallandar, O.B., Evenden, J., Alifui-Segbaya, F., Ahmed, KE.: **Accuracy of 3-dimensionally printed full-arch dental models: A systematic review.** J Clin Med. (2020), 9(10): 3357, DOI: 10.3390/jcm9103357.
- [14] Prochazka A., Dostalova T., Kasparova M., Vysata O., Charvatova H., Sanei S., Marik V.: **Augmented reality implementations in stomatology.** Applied Sciences (2019), 9, 2929: pp. 1-13. DOI: 10.3390/app.9142929
- [15] Procházka A., Kašparová M., Yadollahi M., Vyšata O., Grajciarová J.: **Multi-camera systems use for dental arch shape measurement.** SPRINGER: The Visual Computer, (2015, 2014), 31: pp. 1501-1509, DOI: 10.1007/s00371-014-1029-z.
- [16] Yadollahi M., Prochazka A., Kasparova M., Vysata O.: **The use of combined illumination in segmentation of orthodontic bodies.** SPRINGER: Signal, Image and Video Processing, SIViP (2015) 9: pp. 243-250, DOI: 10.1007/s11760-014-0653-4.

Optical Imaging Modalities for the Detection of Head and Neck Cancer Margins

Ethan J. Han¹; Luran K. Evans¹; Yazeed Alhiyari¹; Christian Wooten¹; Brandon Mo¹; Maie A. St. John^{1,2}

1. Department of Head and Neck Surgery, University of California, Los Angeles, CA, USA
2. Jonsson Comprehensive Cancer Center, University of California, Los Angeles, CA, USA

ABSTRACT

Positive surgical margins in head and neck cancers (HNC) are associated with poor survival. Standard frozen section analysis for intraoperative assessment of margins is limited by processing time and sampling error. Optical imaging technologies may address these limitations. We identified the following techniques in a literature search of optical imaging modalities for the detection of head and neck tumor margins: autofluorescence imaging, dynamic optical contrast imaging, optical coherence tomography, narrow band imaging, hyperspectral imaging, Raman spectroscopy, near-infrared fluorescence imaging, confocal laser endomicroscopy, and high-resolution microendoscopy. Penetration depths range from surface level to 6 mm, image acquisition times range from real-time to several minutes, and 3/9 require exogenous contrast agents. Reported sensitivity and specificity range from 71-100% and 43-100%, respectively. Each reviewed modality lends unique strengths such as fast image acquisition times, wide field of view, high native contrast, or seamless integration with existing endoscopes. However, none have yet to replace palpation and frozen section analysis in the operating room.

Keywords: optical imaging, margin detection, head and neck cancer, review, fluorescence imaging, spectroscopy, microscopy

1. INTRODUCTION

The global incidence of head and neck cancers (HNC) is steadily increasing with over 50,000 new cases projected in the U.S. in 2023 alone.^{1,2} Despite the widespread use of chemoradiation and the emergence of targeted therapeutics, surgery remains the primary treatment for many HNC.³ Successful HNC resection hinges on precise delineation of tumor margins to minimize morbidity and reduce risk of recurrence.⁴ Currently, surgeons rely on pre-operative imaging, palpation, and expertise to guide the initial resection, followed by frozen section analysis. While effective, this process is time-consuming, especially if initial margins return positive, necessitating additional resection and sending more frozen sections. Furthermore, frozen section analysis is subject to sampling error, leading to missed tumor.⁵

Recent strides in optical imaging technologies present opportunities for accurate and timely assessment of tumor margins. This paper reviews various optical techniques including, autofluorescence imaging (AFI), fluorescent lifetime imaging (FLIM), dynamic optical contrast imaging (DOCI), targeted fluorescent probes, high-resolution microendoscopy (HRME), narrow band imaging (NBI), optical coherence tomography (OCT), confocal laser endomicroscopy (CLE), hyperspectral imaging (HSI), and Raman spectroscopy (RS), highlighting their clinical utility in detecting HNC margins.

2. METHODOLOGY

A systematic search of the literature was performed using the PubMed, Embase, and Web of Science databases. Search terms included “head and neck,” “salivary,” “oral,” “nasopharynx,” “oropharynx,” “pharynx,” “larynx” in permutations with “cancer,” “malignancy,” “neoplasm,” “imaging” and “margin.” Duplicates were removed and both abstracts and full text were screened by two independent reviewers for inclusion.

3. RESULTS

A summary of the attributes and specifications of the reviewed technologies is shown in **Table 1**.

Table 1. Attributes and Specifications of Different Optical Imaging Modalities

Modality	Detection Mechanism	Target	Contrast Agents	Excitation Wavelength	FOV	Image Time	Max Depth	Sensitivity (%)	Specificity (%)	Advantages/Disadvantages
Narrow Band Imaging (NBI)	Auto-fluorescence	Hemoglobin	None	415 nm, 540 nm	2-100 mm depth of field, 160-170° FOV	Real-Time	Superficial 150-300 µm	73-100	64-89	(+) adaptable with current endoscopes, rapid image acquisition (-) training to interpret images, limited tissue penetration, signal obscured by blood on surgical field
Autofluorescence Imaging (AFI)	Auto-fluorescence	Endogenous fluorophores	None	400-480 nm	Widefield (44 mm diameter)	Real-Time	Superficial	91	100	(+) widefield, label-free imaging (-) lower tissue contrast, limited tissue penetration
Fluorescence Lifetime Imaging (FLIM) / Dynamic Optical Contrast Imaging (DOCI)	Auto-fluorescence	Endogenous fluorophores	Dual capability	355-357 nm, 370 nm	Widefield (4-10 mm diameter)	2-3 s per spectral band	Superficial	86	87	(+) widefield, label-free imaging, greater fluorophore specificity (-) lower tissue contrast, limited tissue penetration
Near-Infrared Fluorescence (NIR)	Fluorescence	Fluorescent probe	ICG, IRDye-800CW	775-789	Widefield (11.2 x 8.4 cm)	Varies	6mm	71-100	57-98	(+) high tissue contrast, increased imaging depth (-) requires infusion/application of artificial dyes, uptake may be affected by tumor heterogeneity
Hyperspectral Imaging (HSI)	Spectroscopy	Spectral bands	None	450-900 nm	Widefield or Microscopy	60 sec	1-2mm	89-90	90-91	(+) high spatial resolution, rapid image acquisition (-) large amounts of data may be unwieldy, processing algorithms are not optimized
Raman Spectroscopy (RS)	Spectroscopy	Scattered light	None	650-1064 nm	500 x 500 µm	3 min for 7 mm ²	Superficial 100 µm	88-100	91-95	(+) rapid generation of histology-like images (-) data processed through diagnostic model before displayed
Confocal Laser Endomicroscopy (CLE)	Light Reflectance Microscopy	Reflected light	Fluorescein, Patent Blue V	488-660 nm	240 µm diameter	~125 ms	250 µm	74-88	43-80	(+) high-resolution images of cellular architecture (-) small FOV, requires application of artificial dye
High Resolution Microendoscopy (HRME)	Microscopy	Reflected light	Porphyrine	White Light	100 µm diameter	Real-Time	Superficial 50-100 µm	96-98	91-95	(+) low cost, allows for visualization of cellular architecture (-) small FOV, requires application of artificial dye
Optical Coherence Tomography (OCT)	Light reflectance	Reflected light	None	1310 nm	6-7 mm scan plane	100 ms	1-2mm	88-100	70-87	(+) increased imaging depth, label-free and non-invasive (-) extensive training to interpret images, lower resolution

Narrow Band Imaging

Narrow band imaging (NBI) harnesses differences in absorption spectra among tissue types to visualize superficial mucosal and vascular structures. NBI modifies standard white light endoscopes with two optical band pass filters centered at 415 ± 30 nm and 540 ± 30 nm.⁶ The 415 nm filter is centered around the peak absorption of hemoglobin, highlighting superficial capillaries in brown, whereas the 540 nm filter penetrates deeper into the mucosa and enhances contrast between vasculature.⁷⁻⁹ In doing so, NBI allows for the visualization of microvascular patterns associated with dysplastic tissue in HNC, which appear as scattered brown spots upon imaging.⁸⁻¹¹

The utility of NBI has been evaluated in a variety of HNC. Three studies by Tirelli et al. assessed NBI-guided resections in oral cavity and oropharyngeal HNC. The first pilot study included 16 patients with NBI-defined margins that were larger than the white light-delineated (WL) margins.¹² After confirming the presence of histopathologic abnormalities between the NBI and WL margins with frozen section analysis (FS), the surgical margin was extended to the NBI margin. The authors reported sensitivity (Sn), specificity (Sp), positive predictive value (PPV), and negative predictive value (NPV) of 100%, 88.9%, 100%, and 87.5%, respectively. A subsequent study comparing 26 patients undergoing NBI-guided resection and 44 patients undergoing traditional resection found a significant reduction in the rate of positive margins with NBI resection (11.5% vs 36.4%, $p=0.0282$).¹³ The authors repeated the pilot study in a larger cohort of 61 patients and were able to obtain negative resection margins in 80.3% of cases, with a Sn of 94.4%, Sp 64.0%, PPV 79.1%, NPV 88.9%.¹⁴ The use of NBI prolonged operating time by an average of 5 minutes. Klimza et al. found NBI to be a useful adjunct with margin sampling methods in oral HNC, demonstrating a PPV of 100% and NPV 96.43% when NBI was combined with “O’clock” FS margin sampling.¹⁵ NBI can also be adapted for transoral robotic surgery (TORS) procedures. In a prospective study evaluating 61 patients undergoing TORS-resection of oral/oropharyngeal HNC, Vicini et al. reported a higher rate of negative superficial lateral margins when using NBI intraoperatively (87.9% with NBI vs 57.9% without NBI, $p=0.02$).¹⁶ Vicini et al. and Tirelli’s groups both note NBI cannot be used to assess the deep resection margin given its limited tissue penetration depth. Blood in the surgical field will also obscure the NBI picture since it is highly concentrated with hemoglobin.^{12,16}

The use of NBI is well-documented in the examination of laryngeal lesions. Ni et al. was the first to classify NBI microvascular patterns in the larynx, describing brown speckles or tortuous, line-like shapes when viewing malignant lesions with NBI.⁹ This allows for delineation of tumor boundaries prior to resection, reducing the risk of leaving positive margins. Indeed, another study by the Klimza et al. group reported improved accuracy of laryngeal cancer discrimination with NBI compared to WL endoscopy.¹⁷ Garofolo et al. showed a significant reduction in rates of positive superficial margins with NBI-guided transoral laser surgery (TOLS) in glottic cancer (3.6% with NBI vs. 23.7% without NBI, $p<0.001$). In a randomized controlled trial of 113 patients receiving TOLS for glottic carcinoma, Zwakenberg et al. also found a lower rate of positive margins with NBI-TOLS, along with a non-statistically significant improvement in recurrence-free survival at study termination (83% vs 71%, $p=0.08$).¹⁸

NBI has demonstrated utility in the delineation of superficial resection margins, increasing the rate of negative margin resections in a variety of HNC.^{13,16,18-20} It is integrable with standard endoscopes and adds minimal time to operating time.

Autofluorescence Imaging

Autofluorescence imaging (AFI) has garnered considerable interest for its potential for real-time, noninvasive evaluation of tumor margins. This technique interrogates tissue composition by measuring the emission of endogenous fluorophores, such as NADH and FAD, following excitation by an external light source.²¹ Within tumors, metabolic derangements coupled with changes to stromal and cellular architecture modifies the autofluorescence signal, commonly leading to a loss of autofluorescence.^{22,23} AFI allows for visualization of HNC margins and may also prove beneficial in the early detection of dysplastic tissue.²⁴

In 2006, Lane et al. documented one of the earliest uses of AFI in HNC, developing a handheld device for the detection of autofluorescence loss (AFL) in high-risk oral lesions. Their device, later marketed as VELscope®, was able to discriminate between normal oral mucosa, severe dysplasia, and oral squamous cell carcinoma (OSCC) with Sn 98% and

Sp 100%.²² Ohnishi et al. reported similar results when evaluating OSCC tumor margins with VELscope®, attaining Sn 91% and Sp 100%.²⁴ Poh et al. also used VELscope® to successfully identify 32/33 (97%) of dysplastic or cancerous biopsies in OSCC margins.²⁵ Significant extension of AFL beyond the clinically apparent boundary ranging from 4-25 mm was also present in many cases. The authors found that regions with AFL but normal/low-grade dysplasia on histopathology demonstrated genetic alterations associated with cancer risk on microsatellite analysis. This suggested that AFI could even identify high-risk areas beyond the tumor boundary, allowing for prophylactic extension of margins to reduce risk of recurrence.

Outcomes in AFI-guided resection of oral cancer have been explored in larger cohorts. Another study by Poh et al. observed a significant reduction in 3-year local recurrence rate among 246 patients with oral cancer who underwent VELscope®-guided resection (6.5% AFI-guided vs 40.6% traditional).²⁶ This was corroborated on multivariate analysis, which identified AFI-guided resection as a strong independent predictor of regional failure (Hazard Ratio 0.16, 95% CI 0.06-0.39, $p < .001$). However, a randomized clinical trial of 443 patients undergoing VELscope®-guided resection of oral cancer by Durham et al. found no significant differences in failure of first-pass margins, regional failure, disease-specific survival, or overall survival between the AFI-guided and WL-guided groups.²⁷ The authors noted that AFI is less suitable for evaluation of the deep margin in oral malignancies, which may contribute to recurrence if not properly cleared.

Fluorescence Lifetime Imaging and Dynamic Optical Contrast Imaging

Fluorescence lifetime imaging (FLIM) leverages the autofluorescence of endogenous fluorophores similarly to AFI but measures the temporal decay of fluorophores rather than their emission intensities within tissues. This allows for discrimination between fluorophores with similar or overlapping emission spectra.²⁸

Sun et al. described the use of a fully-integrated FLIM endoscope in 2013, which was used to image 10 patients with suspected OSCC.²⁹ Tumors had both lower fluorescent intensities and shorter lifetimes than normal tissue using a single bandpass filter centered at the emission peak of NADH. These findings were largely corroborated by Duran-Sierra et al. using a FLIM endoscope to image the oral cavity of 39 patients with oral lesions, measuring lower emission intensities and shorter decays at the spectral peaks of NADH and collagen in tumors.³⁰ Marsden et al. also observed similar temporal dynamics when testing FLIM for intraoperative margin assessment in 53 patients undergoing oral cancer resection.³¹ Their machine learning-augmented analysis successfully classified healthy and cancerous tissue with a Sn of 86% and Sp 87%.

Dynamic optical contrast imaging (DOCI) compares the temporal dynamics of fluorophore decay states with their steady-state emission after excitation. By using this normalization approach, DOCI captures similar fluorescence lifetime data as FLIM but without the long acquisition times or complex post-processing.³²⁻³⁴ Tajudeen et al. demonstrated that DOCI could differentiate between tumor, muscle, fat, and collagen in a pilot study of 15 patients with head and neck SCC.³⁴ In a subsequent study, Tam et al. overlaid DOCI images over the WL view, creating a visual map of margins for DOCI-guided resection.³⁵ DOCI images correlated well with histology, with tumor displaying lower DOCI values (shorter lifetime) than normal surrounding mucosa.

Fluorescent Probes

Fluorescent probes have emerged as promising tools for the detection of HNC margins, offering improved imaging depth and stronger imaging contrast compared to other optical methods.²¹ These fluorescent agents usually operate within the near-infrared spectrum (>750 nm), allowing for greater tissue penetration than ultraviolet or visible light and reduced signal interference from background autofluorescence.³⁶

Indocyanine green (ICG) was the first fluorescent contrast agent approved by the FDA and has been utilized in the detection of surgical margins in a variety of malignancies including liver, breast, and colorectal cancers.³⁷⁻³⁹ Administered intravenously, ICG demonstrates enhanced uptake in tumor cells, allowing for the delineation of cancerous tissue. Pan et al. explored the utility of ICG-guided intraoperative resection of OSCC in a prospective trial of 20 patients.⁴⁰ ICG fluorescence identified the tumor border in all patients, and imaging of the tumor bed post-resection found four patients with abnormal residual fluorescence, driving additional resection. Two of those cases had positive

margins on histopathological analysis, confirming that ICG fluorescence could detect subclinical margins. However, ICG is not tumor-specific, as ICG-accumulation can occur in physiological states associated with increased vascular permeability such as inflammation. Indeed, pathology evaluation of the two-false positives in Pan et al.'s study revealed inflammatory cell infiltration. Nonetheless, Wu et al. recognized the potential benefits of ICG in a retrospective cohort study of 13 patients, finding lower rates of positive margins in ICG-guided resection margin tissue compared to a non-ICG cohort (0.78% vs 6.25%, $p < 0.05$).⁴¹

5-aminolevulinic acid (5-ALA) is a heme synthesis pathway precursor that selectively accumulates in tumor cells and is converted into its fluorescent metabolite, protoporphyrin IX (PPIX).⁴² PPIX emits a red fluorescence with a peak centered at 634 nm and can be used simultaneously with AFI.^{43,44} In a study by Leunig et al., 5-ALA was topically applied to patients with suspected OSCC, identifying severe dysplasia and OSCC with a Sn of 99%, Sp 60%, PPV 77.3%, NPV 97.5%.⁴⁴ While 5-ALA detects oral cavity malignancies with high sensitivity, its performance is still complicated by its lower specificity. Furthermore, its emission peak is outside the near-infrared spectrum, reducing tissue penetration.

Targeted Fluorescent Probes

The development of immunofluorescent probes offers the same tissue penetration and signal to background contrast as unconjugated fluorescent dyes but with the ability to target cancer-specific biomolecules. A targeted fluorescent probe is composed of a fluorescent dye conjugated to a targeting moiety, which have included antibodies, peptides, and polymers.²¹ Many cancer-related targets have been explored in HNC, including a variety of cell membrane receptors, cellular enzymes, and tumor pH.

The use of epidermal growth factor receptor (EGFR) targeted fluorescent probes, cetuximab-800CW and panitumumab IRDye800CW, has been extensively explored for the evaluation of HNC margins. EGFR is expressed in up to 80-90% of HNSCC, making it an ideal target for immunofluorescence.⁴⁵ Voskuil et al. performed a phase I clinical study in 15 patients with HNSCC, identifying all positive resection margins with cetuximab-800CW and yielding a Sn 100% and Sp 91%. Furthermore, 96% of tumor sections were EGFR-positive, confirming that a cetuximab targeting moiety was appropriate for HNSCC.⁴⁶ A phase II study by the same group in 65 HNSCC patients reported cetuximab-800CW identified positive margins with a Sn of 100%, Sp 85.9%, PPV 58.3%, and NPV 100.0% and close 1-3 mm margins with a Sn of 79.2%, Sp 76.1%, PPV 52.7%, and NPV 91.5%.⁴⁷ Trials with panitumumab IRDye800CW have also demonstrated similar performance in margin assessment. Fakurnejad et al. previously observed in a pilot study of 11 patients that fluorescent intensity of panitumumab IRDye800CW increased proportionally with the level of dysplasia in HNSCC.⁴⁸ Their subsequent phase I study in 29 patients showed that the margin with the highest fluorescent intensity corresponded to the closest margin on histopathology.⁴⁹ This group also compared interobserver agreement on the location of tumor margins between pathology (ground truth) and the operating surgeon or the panitumumab IRDye800CW-generated fluorescence map, finding that fluorescence ($R^2 = 0.98$) demonstrated better correlation with pathology than the surgeon ($R^2 = 0.75$).⁵⁰

Rapid development and success of targeted probes has spurred interest in other targets including protein biomarkers and cellular enzymes overexpressed in HNSCC, along with markers indicating alterations in the tumor microenvironment. Wang et al. reported the use of a topically-applied, c-MET targeted ICG probe that was administered to 10 OSCC patients and provided intraoperative detection of tumor with Sn 71%, Sp 83%, PPV 83%, and NPV 73%.⁵¹ Another group tested an integrin $\alpha\beta6$ -targeting peptide for the intraoperative evaluation of SCC bony margins in a first study of its kind, yielding a Sn of 100%, Sp 98.3%, PPV 92.06%, and NPV 100%.⁵² Cellular pH changes due to cancer metabolism have also been of interest in the target probe pipeline, with Voskuil et al. demonstrating the ability of a pH-activated fluorescent nanoprobe to detect tumor-positive resection margins in a variety of cancers including HNSCC.⁵³ While, these newer moieties offer a diversity of targets that can be exploited in HNC, they are, however, relatively understudied and lack validation in the larger phase II trials that have been conducted with EGFR probes.

High-Resolution Microendoscopy

High-resolution microendoscopy (HRME) provides assessment of clinical margins without the high cost associated with other imaging devices. HRME is optically simple and serves as a portable fluorescent microscope, utilizing a fiber optic

imaging probe to survey tissue topically stained with a fluorescent contrast agent (e.g. proflavine).⁵⁴ This allows the user to observe the cellular architecture of a surgical margin with microscopic definition, identifying features associated with malignancy such as enlarged nuclear size and increased nuclear-to-cytoplasmic ratio.⁵⁵ The versatility and compact design of HRME have facilitated its deployment across a spectrum of anatomical sites, spanning from HNC to esophageal squamous cell neoplasia, as well as HPV-associated cervical and anal cancers.⁵⁴⁻⁵⁸

In 2012, Vila et al. demonstrated the feasibility of HRME in the discrimination of benign and malignant mucosa in ex-vivo HNSCC specimens from 38 patients, achieving a Sn 98.3% and Sp 90.9% with high interobserver reliability.⁵⁵ Miles et al. then applied HRME to the visual intraoperative margin in 33 HNSCC patients, displaying HRME-generated images to blinded observers.⁵⁴ Using histopathology as the gold standard, HRME demonstrated Sn 96%, Sp 95%, PPV 91%, NPV 98% when identifying positive margins.

The strengths of HRME lie in its low cost, high reported Sn and Sp, ease of use, and ability to analyze the operative margin with microscopic resolution. The price of a single unit is reportedly less than \$5000, and observers can be quickly trained to interpret HRME images.⁵⁴

Confocal Laser Endomicroscopy

Confocal laser endomicroscopy (CLE) has been extensively researched in gastroenterology for the assessment of mucosal histology but has also shown promise in HNC.^{59,60} CLE is based on the principles of confocal laser scanning microscopy, where tissue is illuminated with a low-power laser and only reflected light from single planes of interest are captured. This generates high-resolution, sectional images of the sample, allowing for assessment of cellular architecture and histological diagnosis. Topical fluorescent agents can also be applied to the tissue to enhance contrast. CLE utilizes a handheld probe coupled with a laser unit to scan the target tissue, identifying regions containing unorganized cellular architecture, irregular cell morphology, contrast leakage, and other indicators of malignant transformation.⁶⁰

CLE has been used to evaluate HNC margins in both the oral cavity and larynx. Dittberner et al. conducted a pilot study in 13 patients undergoing oral HNC resection and found that CLE with topical fluorescein identified HNSCC with Sn 87.5% and Sp 80.0%.⁶¹ Their system had a FOV of 475x267 μm and scanning depth of 250 μm , with image acquisition averaging 9 minutes. Sievert et al. used a similar approach with a smaller probe (FOV 240 μm) and intravenous fluorescein in 8 patients with laryngeal SCC, calculating a Sn 72.3%, Sp 87.9%, PPV 85.7%, NPV 76.1%.⁶² A larger study by Abbaci et al. imaged 42 patients with oral or laryngeal cancer using CLE with topical patent blue V dye, with Sn 73.2-75% and Sp 30-57.4% ranging across different providers.⁶³

CLE allows for rapid optical biopsy of clinical margins, creating high-resolution images of cellular architecture. In-vivo applications of this technology in HNC have still been a relatively recent development, and reported limitations include high cost, limited FOV, low specificity of fluorescent agents, and standardization of image interpretation.⁶⁰⁻⁶³

Optical Coherence Tomography

Optical coherence tomography (OCT) measures the interference of reflected light to produce cross-sectional images of tissues, akin to ultrasound but employing light rather than sound. With established applications in cardiology and ophthalmology for coronary artery and retinal imaging, the versatility of OCT has spurred interest in its potential for imaging head and neck cancer margins. OCT is non-invasive and offers high-resolution visualization of tissue layers and submucosal structures without the need of any tissue preparation or contrast agents.⁶⁴ Its imaging depth extends to 1-2 mm, enabling observation of tissue architecture that may be disrupted in malignancy.

In 2006, Armstrong et al. were among the first to apply OCT to HNC, imaging 22 patients with suspected laryngeal cancer and achieving an average imaging depth of 0.65 mm with 10 μm resolution.⁶⁵ Imaged regions positive for invasive cancer demonstrated loss of the demarcation between the epithelium and the submucosal tissue, as well as progressive thickening of the epithelial layer. A decade later, Hamdoon et al. used OCT to identify oral cancer margins with an average Sn 81.5%, Sp 87%, PPV 61.5%, NPV 95%.⁶⁶ Sunny et al. achieved Sn 100% Sp 100% in identifying malignancy and Sn 92.5% Sp 68.8% in identifying dysplasia at the clinical margin of 14 OSCC patients undergoing resection.⁶⁷

Raman Spectroscopy

Raman spectroscopy (RS) is another label-free technique of interest for the assessment of surgical margins. RS relies on the inelastic scattering of a laser light source as it interacts with the molecular vibrations within a sample. The resulting spectroscopic peaks reflect the sample's molecular composition, which may change due to cancer-associated alterations in proteins, DNA, or other biomolecules. RS can also be combined with microscopy in a technique called stimulated Raman histology (SRH) to image specific molecular bonds and generate a histology-like image representing the spectroscopic data.

Studies of RS have attempted to leverage a diversity of spectral peaks to differentiate normal and malignant tissue. In 2016, Cals et al. performed ex-vivo RS on OSCC tissue from 10 patients and developed a tissue classification model that could distinguish between OSCC and non-tumorous tissue with 86% accuracy.⁶⁸ They noted, however, that the image acquisition time was too lengthy to potentially replace frozen sections. Thus, focusing on specific Raman shifts using SRH could reduce imaging time while maintaining diagnostic capability. Hoesli et al. imaged 50 HNC patients at the 2845 cm^{-1} and 2940 cm^{-1} spectral bands, which correspond to CH_2 and CH_3 bonds respectively.⁶⁹ CH_2 bonds highlight lipids while CH_3 bonds predominate in proteins and DNA. Image acquisition was <30 seconds and the resulting SRH images were read by a blinded pathologist with Sn 88.1% Sp 95.2%. Steybe et al. performed a similar evaluation in 8 OSCC patients, detecting OSCC with Sn 100%, Sp 90.91%, PPV 90%, NPV 100%.⁷⁰ They were also able to further subclassify non-neoplastic tissues into muscle, connective tissue, adipose, and lymph node. Image acquisition times were longer than frozen sections, however the authors noted that RM could be performed in the operating room, eliminating the need for sample transfer to pathology. Assessing water content through RS may also be an effective measure of tissue malignancy. Barroso et al. determined the water concentration of OSCC resection specimens by calculating the ratio of the $-\text{OH}$ (3390 cm^{-1}) and CH_3 (2935 cm^{-1}) Raman bands. They found the water concentration of OSCC was significantly greater than surrounding normal tissue, and a cutoff concentration of 69% classified OSCC with Sn 99% Sp 92%.⁷¹

RS gathers a wealth of spectroscopic data, enabling label-free and non-invasive molecular characterization of tissues. This is a unique feature of RS that allows it to capture actual data on the biochemical composition of a sample that reflects the histological changes that occur in malignancy.

Hyperspectral Imaging

Hyperspectral imaging (HSI) generates a three-dimensional data cube where each pixel of a spatially-resolved image contains spectral data across a wide range of wavelengths. Thus, HSI captures a vast amount of information regarding the scattering and absorption of electromagnetic radiation as it encounters a target tissue, revealing its structural and molecular composition. Data can be processed through varying diagnostic and feature extraction models, identifying aberrations in the spectral signature to differentiate tumor from benign tissue.

Fei et al. was the first to apply HSI to the assessment of HNC surgical margins, imaging 14 patients with oral, laryngeal, and thyroid tumors.⁷² Autofluorescence imaging and fluorescence imaging with proflavine and 2-NBDG dye were also performed for comparison. Data cubes were processed through a machine-learning algorithm for feature extraction and image classification, distinguishing tumor from normal tissue with Sn 90% Sp 91% in the oral cavity and Sn 94% Sp 95% in the thyroid. HSI outperformed both proflavine and 2-NBDG fluorescence imaging in this study (oral cavity accuracy 90% HSI vs 80% autofluorescence vs 83% 2-NBDG vs 70% proflavine). A follow-up study by their group utilized a similar protocol to image 36 HNC patients, also achieving greater accuracy with HSI compared to autofluorescence and fluorescence imaging.⁷³ Machine learning can also augment HSI diagnosis—Halicek et al. found that HSI image analysis from 102 HNSCC patients with a convolutional neural network model demonstrated superior accuracy at identifying the surgical margin compared to autofluorescence and fluorescence imaging when applied to traditional SCC tissue. However, autofluorescence outperformed HSI and fluorescence imaging at identifying HPV+ SCC margins.⁷⁴ Image acquisition was rapid, averaging one minute with 35 seconds for image classification.

4. DISCUSSION

The current standard method for intraoperative assessment of HNC margins, frozen section analysis, faces challenges such as prolonged processing times, dependency on specialized pathology services, low sensitivity, and limited ability to

evaluate the tumor bed.⁷⁵ Notably, up to 22% of initially negative frozen margins may exhibit close or positive margins upon final pathology, carrying significant implications for patient survival, particularly given the high recurrence risk associated with positive surgical margins.^{4,76} To address these drawbacks, there is a growing interest in optical imaging technologies to improve resection accuracy and reduce positive margin rates. For these emerging modalities to gain widespread acceptance in surgical settings, they must not only demonstrate comparable or superior accuracy to frozen sections but also streamline the margin evaluation process. Essential capabilities include fast image acquisition and display times, a wide field of view for comprehensive margin capture, high contrast for effective tissue differentiation, and user-friendly integration into existing surgical workflows. This review provides an overview of optical imaging technologies for assessing HNC margins, categorizing them based on their mechanisms of detection, including fluorescence-based technologies (NBI, AFI, DOCI/FLIM, and NIR fluorescent probes), spectroscopy-based techniques (Raman spectroscopy and HSI), microscopy-based modalities (CLE and HRME), and OCT, which is uniquely based on light reflectance and is discussed separately.

Fluorescence-based imaging modalities generally provide rapid image acquisition and widefield capabilities, allowing for the assessment of entire margins. NBI has been the most well-studied fluorescence-based imaging modality, and its adoption as a tool has been facilitated by its integration into conventional white light endoscopes. Classification systems for of NBI microvascular patterns have also been published, although there is an associated learning curve.⁹ Despite its efficacy, the NBI is confounded by the presence of hemoglobin-containing blood on the surgical field, reducing its intraoperative effectiveness once an incision has been made. Commercialized AFI devices such as VELscope® expand the measured emission spectra and have demonstrated ability to delineate OSCC margins and identify premalignant lesions.²⁵ Nonetheless, widening the emission passband lowers AFI specificity due to loss of ability to distinguish specific fluorophores. FLIM offers greater specificity by measuring fluorescence decay over several spectral bands, albeit with longer image acquisition and processing times, although DOCI can expediate this process with a simpler ratio-metric approach. All the aforementioned methods rely on autofluorescence of endogenous fluorophores, as such their shared limitation is imaging depth. Emission of native fluorescence occurs at shorter wavelengths, limiting imaging depth to ~300µm. In contrast, untargeted and targeted fluorescent probes operating in the NIR spectrum, increase tissue penetration up to 6 mm.⁴⁹ The earlier untargeted probes faced poor tissue specificity, and uptake was confounded by inflammation.⁴⁰ However, targeted probes have significantly mitigated these issues by providing the capability to specifically target biomarkers unique to HNC. The EGFR-targeted probes, cetuximab-800CW and panitumumab IRDye800CW, have been particularly well-characterized in several clinical trials and accurately delineated tumor margins in these studies with high signal to tumor background ratio. Despite their advantages, these probes require intravenous infusion days before surgery for optimal uptake, and assessing the depth of observed fluorescence remains challenging due to limitations of current fluorescence imaging cameras.

Spectroscopic methods allow the user to query the molecular composition of a sample and identify biochemical changes associated with malignancy. RS is the most well-studied technique and can be used alone or in combination with microscopy (SRH). When used independently without microscopy, RS data must be processed through a diagnostic model for classification. In contrast, SRH provides a visual representation of the spectral data in a histology-like image, where each pixel corresponds to the intensity of the Raman signal. HSI captures even more data, gathering spatially-resolved spectral information across hundreds of spectral bands. Regardless, in most use cases, spectroscopic data is interpreted by a classification model to distinguish tumor and normal tissue. While this may be less favorable for the operating surgeon compared to a technique that is inherently interpretable, it's worth noting that SRH images, despite not requiring model interpretation, still demand training for accurate interpretation. Moreover, the commercial introduction of SRH and HSI systems is relatively recent, and the associated costs may currently hinder widespread implementation in the operating room. Ongoing efforts include the development of fiber-optic probes for in-vivo spectroscopy and diagnostic models with automatic feature extraction, but further studies are essential to validate the efficacy of spectroscopic techniques and assess their potential for integration into the surgical workflow.^{76,77}

Microscopy-based techniques visualize the surgical margin with cellular resolution to determine malignancy potential. HRME is a low-cost, optically-simple microscopy device that may offer enhanced margin assessment in under-resourced settings. The price of a single unit is reportedly less than \$5000, and observers can be quickly trained to interpret HRME images.⁵⁴ CLE utilizes laser excitation to produce higher-resolution images, but CLE devices can cost upwards of \$100,000 and are currently marketed for gastroenterology applications, which has led to issues with adapting the CLE probes for HNC use.⁶⁰ Studies of microscopy techniques describe limitations such as small FOV, limited tissue

penetration, artifact in irradiated tissues, and reliance on topical contrast agents. Additionally, common contrast agents such as proflavine are relatively non-specific, creating imaging artifact when the dyes mix with saliva, blood, or are taken up by non-cancerous tissues.^{60,63} Nonetheless, efforts are underway to develop microscopy systems compatible with EGFR targeted probes.^{54,55} The main practical limitation of microscopy techniques is the small FOV, which prevents evaluation of whole margins. Regardless, microscopy may fulfill an unmet need, providing microscopic assessment of margins in conjunction with a widefield device.

OCT allows for clear visualization of structural tissue changes associated with malignancy and possesses superior penetration depth compared to other label-free methods. It has been well-characterized for ophthalmologic and cardiac applications, thus the technology has been well known to be translated into HNC applications. Image noise and lower image resolution have been cited as limitations of OCT for margin imaging. Extensive user training is the most frequently documented limitation of OCT, as OCT images do not resemble conventional imaging and there are no standardized libraries for OCT interpretation.⁶⁴ Artificial intelligence and diagnostic algorithms for automatic feature extraction and interpretation are emerging to address this need, however.⁷⁸⁻⁸⁰

5. CONCLUSION

Optical imaging holds significant promise for real-time, non-invasive determination of HNC, and each modality brings a unique set of capabilities that significantly improve the margin assessment process compared to traditional frozen sections. However, no single modality has yet to replace standard palpation and frozen section analysis in the operating room. To do so, optical imaging techniques must provide fast image acquisition and display times, wide FOV for capturing whole margins, high contrast for tumor/tissue types, and integration with existing surgical workflow.

ACKNOWLEDGEMENTS

We thank Dr. Ramesh Shori (University of California, Los Angeles) for his guidance and comments on the manuscript.

REFERENCES

1. Gormley M, Creaney G, Schache A, Ingarfield K, Conway DI. Reviewing the epidemiology of head and neck cancer: definitions, trends and risk factors. *Br Dent J*. Nov 2022;233(9):780-786. doi:10.1038/s41415-022-5166-x
2. Siegel RL, Miller KD, Wagle NS, Jemal A. Cancer statistics, 2023. *CA Cancer J Clin*. Jan 2023;73(1):17-48. doi:10.3322/caac.21763
3. Bozec A, Culie D, Poissonnet G, Dassonville O. Current role of primary surgical treatment in patients with head and neck squamous cell carcinoma. *Curr Opin Oncol*. May 2019;31(3):138-145. doi:10.1097/CCO.0000000000000531
4. Eldeeb H, Macmillan C, Elwell C, Hammod A. The effect of the surgical margins on the outcome of patients with head and neck squamous cell carcinoma: single institution experience. *Cancer Biol Med*. Mar 2012;9(1):29-33. doi:10.3969/j.issn.2095-3941.2012.01.005
5. Olson SM, Hussaini M, Lewis JS, Jr. Frozen section analysis of margins for head and neck tumor resections: reduction of sampling errors with a third histologic level. *Mod Pathol*. May 2011;24(5):665-70. doi:10.1038/modpathol.2010.233
6. Barbeiro S, Libanio D, Castro R, Dinis-Ribeiro M, Pimentel-Nunes P. Narrow-Band Imaging: Clinical Application in Gastrointestinal Endoscopy. *GE Port J Gastroenterol*. Dec 2018;26(1):40-53. doi:10.1159/000487470
7. Gono K, Obi T, Yamaguchi M, et al. Appearance of enhanced tissue features in narrow-band endoscopic imaging. *J Biomed Opt*. May-Jun 2004;9(3):568-77. doi:10.1117/1.1695563
8. Cosway B, Drinnan M, Paleri V. Narrow band imaging for the diagnosis of head and neck squamous cell carcinoma: A systematic review. *Head Neck*. Apr 2016;38 Suppl 1:E2358-67. doi:10.1002/hed.24300
9. Ni XG, He S, Xu ZG, et al. Endoscopic diagnosis of laryngeal cancer and precancerous lesions by narrow band imaging. *J Laryngol Otol*. Mar 2011;125(3):288-96. doi:10.1017/S0022215110002033
10. Johnstone S, Logan RM. The role of vascular endothelial growth factor (VEGF) in oral dysplasia and oral squamous cell carcinoma. *Oral Oncol*. Apr 2006;42(4):337-42. doi:10.1016/j.oraloncology.2005.06.020
11. Muto M, Nakane M, Katada C, et al. Squamous cell carcinoma in situ at oropharyngeal and hypopharyngeal mucosal sites. *Cancer*. Sep 15 2004;101(6):1375-1381. doi:10.1002/cncr.20482

12. Tirelli G, Piovesana M, Gatto A, Tofanelli M, Biasotto M, Nata FB. Narrow band imaging in the intra-operative definition of resection margins in oral cavity and oropharyngeal cancer. Article. *Oral Oncol.* Oct 2015;51(10):908-913. doi:10.1016/j.oraloncology.2015.07.005
13. Tirelli G, Piovesana M, Gatto A, Torelli L, Nata FB. Is NBI-Guided Resection a Breakthrough for Achieving Adequate Resection Margins in Oral and Oropharyngeal Squamous Cell Carcinoma? Article. *Ann Otol Rhinol Laryngol.* Jul 2016;125(7):596-601. doi:10.1177/0003489416641428
14. Tirelli G, Piovesana M, Marcuzzo AV, et al. Tailored resections in oral and oropharyngeal cancer using narrow band imaging. Article. *Am J Otolaryngol.* Mar-Apr 2018;39(2):197-203. doi:10.1016/j.amjoto.2017.11.004
15. Klimza H, Greczka G, Grabowski L, Majewski P, Banaszewski J, Wierzbicka M. Intraoperative margins in oral and oropharyngeal cancer transoral surgery benefit from sampling method modifications. Article. *Pol J Otolaryngol.* 2022;76(6):37-43. doi:10.5604/01.3001.0015.9678
16. Vicini C, Montevecchi F, D'Agostino G, De Vito A, Meccariello G. A novel approach emphasising intra-operative superficial margin enhancement of head-neck tumours with narrow-band imaging in transoral robotic surgery. Article. *Acta Otorhinolaryngol Ital.* Jun 2015;35(3):157-161.
17. Klimza H, Jackowska J, Piazza C, Banaszewski J, Wierzbicka M. The role of intraoperative narrow-band imaging in transoral laser microsurgery for early and moderately advanced glottic cancer. Article. *Braz J Otorhinolaryngol.* Mar-Apr 2019;85(2):228-236. doi:10.1016/j.bjorl.2018.01.004
18. Zwakenberg MA, Westra JM, Halmos GB, Wedman J, van der Laan B, Plaat BEC. Narrow-Band Imaging in Transoral Laser Surgery for Early Glottic Cancer: A Randomized Controlled Trial. Article; Early Access. *Otolaryngol Head Neck Surg.* 2023 Feb 2023;9. doi:10.1002/ohn.307
19. Sifrer R, Urbancic J, Strojjan P, Anicin A, Zargi M. The Assessment of Mucosal Surgical Margins in Head and Neck Cancer Surgery With Narrow Band Imaging. Article. *Laryngoscope.* Jul 2017;127(7):1577-1582. doi:10.1002/lary.26405
20. Garofolo S, Piazza C, Del Bon F, et al. Intraoperative Narrow Band Imaging Better Delineates Superficial Resection Margins During Transoral Laser Microsurgery for Early Glottic Cancer. Article; Proceedings Paper. *Ann Otol Rhinol Laryngol.* Apr 2015;124(4):294-298. doi:10.1177/0003489414556082
21. Wu CZ, Gleysteen J, Teraphongphom NT, Li Y, Rosenthal E. In-vivo optical imaging in head and neck oncology: basic principles, clinical applications and future directions. Review. *Int J Oral Sci.* Mar 2018;10:13. 10. doi:10.1038/s41368-018-0011-4
22. Lane PM, Gilhuly T, Whitehead P, et al. Simple device for the direct visualization of oral-cavity tissue fluorescence. Article. *J Biomed Opt.* Mar-Apr 2006;11(2):7. 024006. doi:10.1117/1.2193157
23. Burian E, Schulz C, Probst F, et al. Fluorescence based characterization of early oral squamous cell carcinoma using the Visually Enhanced Light Scope technique. Article. *J Cranio-MaxilloFac Surg.* Sep 2017;45(9):1526-1530. doi:10.1016/j.jcms.2017.05.021
24. Ohnishi Y, Fujii T, Ugaki Y, et al. Usefulness of a fluorescence visualization system for the detection of oral precancerous and early cancerous lesions. Article. *Oncol Rep.* 2016;36(1):514-520. doi:10.3892/or.2016.4776
25. Poh CF, Zhang LW, Anderson DW, et al. Fluorescence visualization detection of field alterations in tumor margins of oral cancer patients. Article. *Clin Cancer Res.* Nov 2006;12(22):6716-6722. doi:10.1158/1078-0432.Ccr-06-1317
26. Poh CF, Anderson DW, Scott Durham J, et al. Fluorescence visualization-guided surgery for early-stage oral cancer. Article. *JAMA Otolaryngology - Head and Neck Surgery.* 2016;142(3):209-216. doi:10.1001/jamaoto.2015.3211
27. Durham JS, Brasher P, Anderson DW, et al. Effect of Fluorescence Visualization-Guided Surgery on Local Recurrence of Oral Squamous Cell Carcinoma: A Randomized Clinical Trial. Article. *JAMA Otolaryngology - Head and Neck Surgery.* 2020;146(12):1149-1155. doi:10.1001/jamaoto.2020.3147
28. Datta R, Heaster TM, Sharick JT, Gillette AA, Skala MC. Fluorescence lifetime imaging microscopy: fundamentals and advances in instrumentation, analysis, and applications. *J Biomed Opt.* May 2020;25(7):1-43. doi:10.1117/1.JBO.25.7.071203
29. Sun Y, Phipps JE, Meier J, et al. Endoscopic fluorescence lifetime imaging for in vivo intraoperative diagnosis of oral carcinoma. *Microsc Microanal.* Aug 2013;19(4):791-8. doi:10.1017/s1431927613001530
30. Duran-Sierra E, Cheng S, Cuenca-Martinez R, et al. Clinical label-free biochemical and metabolic fluorescence lifetime endoscopic imaging of precancerous and cancerous oral lesions. Article. *Oral Oncol.* 2020;105doi:10.1016/j.oraloncology.2020.104635

31. Marsden M, Weyers BW, Bec J, et al. Intraoperative Margin Assessment in Oral and Oropharyngeal Cancer Using Label-Free Fluorescence Lifetime Imaging and Machine Learning. Article. *IEEE Trans Biomed Eng.* Mar 2021;68(3):857-868. doi:10.1109/tbme.2020.3010480
32. Kim IA, Taylor ZD, Cheng H, et al. Dynamic Optical Contrast Imaging. *Otolaryngol Head Neck Surg.* Mar 2017;156(3):480-483. doi:10.1177/0194599816686294
33. Kim SW, Song SH, Lee HS, et al. Intraoperative Real-Time Localization of Normal Parathyroid Glands With Autofluorescence Imaging. *J Clin Endocrinol Metab.* Dec 2016;101(12):4646-4652. doi:10.1210/jc.2016-2558
34. Tajudeen BA, Taylor ZD, Garritano J, et al. Dynamic Optical Contrast Imaging as a Novel Modality for Rapidly Distinguishing Head and Neck Squamous Cell Carcinoma from Surrounding Normal Tissue. Article. *Cancer.* Mar 2017;123(5):879-886. doi:10.1002/cncr.30338
35. Tam K, Huang S, Mukdad L, et al. Real-Time Intraoperative Detection of Margins for Oral Cavity Squamous Cell Carcinoma. Article; Early Access. *Otolaryngol Head Neck Surg.* 2023 Jun 2023;3. doi:10.1002/ohn.397
36. de Kleijn BJ, Heldens GTN, Herruer JM, et al. Intraoperative Imaging Techniques to Improve Surgical Resection Margins of Oropharyngeal Squamous Cell Cancer: A Comprehensive Review of Current Literature. Review. *Cancers.* Feb 2023;15(3):25. 896. doi:10.3390/cancers15030896
37. Wakabayashi T, Cacciaguerra AB, Abe Y, et al. Indocyanine Green Fluorescence Navigation in Liver Surgery: A Systematic Review on Dose and Timing of Administration. *Ann Surg.* Jun 1 2022;275(6):1025-1034. doi:10.1097/SLA.0000000000005406
38. Lee EG, Kim SK, Han JH, Lee DE, Jung SY, Lee S. Surgical outcomes of localization using indocyanine green fluorescence in breast conserving surgery: a prospective study. *Sci Rep.* May 11 2021;11(1):9997. doi:10.1038/s41598-021-89423-w
39. Garoufalia Z, Wexner SD. Indocyanine Green Fluorescence Guided Surgery in Colorectal Surgery. *J Clin Med.* Jan 7 2023;12(2)doi:10.3390/jcm12020494
40. Pan JR, Deng H, Hu SQ, et al. Real-time surveillance of surgical margins via ICG-based near-infrared fluorescence imaging in patients with OSCC. Article. *World J Surg Oncol.* May 2020;18(1):8. 96. doi:10.1186/s12957-020-01874-z
41. Wu ZH, Dong YC, Wang YX, Hu QA, Cai HM, Sun GW. Clinical application of indocyanine green fluorescence navigation technology to determine the safe margin of advanced oral squamous cell carcinoma. Article. *Gland Surg.* Feb 2022;11(2):352-357. doi:10.21037/gs-22-33
42. Hadjipanayis CG, Widhalm G, Stummer W. What is the Surgical Benefit of Utilizing 5-Aminolevulinic Acid for Fluorescence-Guided Surgery of Malignant Gliomas? *Neurosurgery.* Nov 2015;77(5):663-673. doi:10.1227/Neu.0000000000000929
43. Alston L, Mahieu-Williams L, Hebert M, et al. Spectral complexity of 5-ALA induced PpIX fluorescence in guided surgery: a clinical study towards the discrimination of healthy tissue and margin boundaries in high and low grade gliomas. *Biomed Opt Express.* May 1 2019;10(5):2478-2492. doi:10.1364/BOE.10.002478
44. Leunig A, Betz CS, Mehlmann M, et al. Detection of squamous cell carcinoma of the oral cavity by imaging 5-aminolevulinic acid-induced protoporphyrin IX fluorescence. Article; Proceedings Paper. *Laryngoscope.* Jan 2000;110(1):78-83. doi:10.1097/00005537-200001000-00015
45. Nair S, Bonner JA, Bredel M. EGFR Mutations in Head and Neck Squamous Cell Carcinoma. *Int J Mol Sci.* Mar 30 2022;23(7)doi:10.3390/ijms23073818
46. Voskuil FJ, de Jongh SJ, Hooghiemstra WTR, et al. Fluorescence-guided imaging for resection margin evaluation in head and neck cancer patients using cetuximab-800CW: A quantitative dose-escalation study. Article. *Theranostics.* 2020;10(9):3994-4005. doi:10.7150/thno.43227
47. de Wit JG, Vonk J, Voskuil FJ, et al. EGFR-targeted fluorescence molecular imaging for intraoperative margin assessment in oral cancer patients: a phase II trial. Article. *Nat Commun.* Aug 2023;14(1):10. 4952. doi:10.1038/s41467-023-40324-8
48. Fakurnejad S, van Keulen S, Nishio N, et al. Fluorescence molecular imaging for identification of high-grade dysplasia in patients with head and neck cancer. Article. *Oral Oncol.* Oct 2019;97:50-55. doi:10.1016/j.oraloncology.2019.08.008
49. Fakurnejad S, Krishnan G, van Keulen S, et al. Intraoperative Molecular Imaging for *ex vivo* Assessment of Peripheral Margins in Oral Squamous Cell Carcinoma. Article. *Front Oncol.* Jan 2020;9:7. 1476. doi:10.3389/fonc.2019.01476

50. Krishnan G, van den Berg NS, Nishio N, et al. Fluorescent Molecular Imaging Can Improve Intraoperative Sentinel Margin Detection in Oral Squamous Cell Carcinoma. Article. *J Nucl Med*. Aug 2022;63(8):1162-1168. doi:10.2967/jnumed.121.262235
51. Wang JB, Li SY, Wang K, et al. A c-MET-Targeted Topical Fluorescent Probe cMBP-ICG Improves Oral Squamous Cell Carcinoma Detection in Humans. Article. *Ann Surg Oncol*. Jan 2023;30(1):641-651. doi:10.1245/s10434-022-12532-x
52. Nieberler M, Stimmer H, Rasthofer D, Nentwig K, Weirich G, Wolff KD. Defining secure surgical bone margins in head and neck squamous cell carcinomas: The diagnostic impact of intraoperative cytological assessment of bone resection margins compared with preoperative imaging. Article. *Oral Oncol*. Mar 2020;102:7. 104579. doi:10.1016/j.oraloncology.2020.104579
53. Voskuil FJ, Steinkamp PJ, Zhao T, et al. Exploiting metabolic acidosis in solid cancers using a tumor-agnostic pH-activatable nanoprobe for fluorescence-guided surgery. Article. *Nat Commun*. Jun 2020;11(1):10. doi:10.1038/s41467-020-16814-4
54. Miles BA, Patsias A, Quang T, Polydorides AD, Richards-Kortum R, Sikora AG. Operative Margin Control With High-Resolution Optical Microendoscopy for Head and Neck Squamous Cell Carcinoma. Article. *Laryngoscope*. Oct 2015;125(10):2308-2316. doi:10.1002/lary.25400
55. Vila PM, Park CW, Pierce MC, et al. Discrimination of Benign and Neoplastic Mucosa with a High-Resolution Microendoscope (HRME) in Head and Neck Cancer. Article. *Ann Surg Oncol*. Oct 2012;19(11):3534-3539. doi:10.1245/s10434-012-2351-1
56. Protano MA, Xu H, Wang G, et al. Low-Cost High-Resolution Microendoscopy for the Detection of Esophageal Squamous Cell Neoplasia: An International Trial. *Gastroenterology*. Aug 2015;149(2):321-329. doi:10.1053/j.gastro.2015.04.055
57. Brenes D, Barberan CJ, Hunt B, et al. Multi-task network for automated analysis of high-resolution endomicroscopy images to detect cervical precancer and cancer. *Comput Med Imaging Graph*. Apr 2022;97:102052. doi:10.1016/j.compmedimag.2022.102052
58. Brenes D, Kortum A, Coole J, et al. Deployment and assessment of a deep learning model for real-time detection of anal precancer with high frame rate high-resolution microendoscopy. *Sci Rep*. Dec 14 2023;13(1):22267. doi:10.1038/s41598-023-49197-9
59. Pilonis ND, Januszewicz W, di Pietro M. Confocal laser endomicroscopy in gastro-intestinal endoscopy: technical aspects and clinical applications. *Transl Gastroent Hep*. Jan 2022;7doi:ARTN 7 10.21037/tgh.2020.04.02
60. Villard A, Breuskin I, Casiraghi O, et al. Confocal laser endomicroscopy and confocal microscopy for head and neck cancer imaging: Recent updates and future perspectives. Article. *Oral Oncol*. Apr 2022;127:8. 105826. doi:10.1016/j.oraloncology.2022.105826
61. Dittberner A, Ziadat R, Hoffmann F, Pertzborn D, Gassler N, Guntinas-Lichius O. Fluorescein-Guided Panendoscopy for Head and Neck Cancer Using Handheld Probe-Based Confocal Laser Endomicroscopy: A Pilot Study. Article. *Front Oncol*. 2021;11doi:10.3389/fonc.2021.671880
62. Sievert M, Oetter N, Aubreville M, et al. Feasibility of intraoperative assessment of safe surgical margins during laryngectomy with confocal laser endomicroscopy: A pilot study. *Auris Nasus Larynx*. Aug 2021;48(4):764-769. doi:10.1016/j.anl.2021.01.005
63. Abbaci M, Casiraghi O, Vergez S, et al. Diagnostic accuracy of in vivo early tumor imaging from probe-based confocal laser endomicroscopy versus histologic examination in head and neck squamous cell carcinoma. Article. *Clin Oral Investig*. Feb 2022;26(2):1823-1833. doi:10.1007/s00784-021-04156-4
64. van Manen L, Dijkstra J, Boccara C, et al. The clinical usefulness of optical coherence tomography during cancer interventions. Review. *J Cancer Res Clin Oncol*. Oct 2018;144(10):1967-1990. doi:10.1007/s00432-018-2690-9
65. Armstrong WB, Ridgway JM, Vokes DE, et al. Optical coherence tomography of laryngeal cancer. Article; Proceedings Paper. *Laryngoscope*. Jul 2006;116(7):1107-1113. doi:10.1097/01.mlg.0000217539.27432.5a
66. Hamdoon Z, Jerjes W, McKenzie G, Jay A, Hopper C. Optical coherence tomography in the assessment of oral squamous cell carcinoma resection margins. *Photodiagnosis Photodyn Ther*. Mar 2016;13:211-217. doi:10.1016/j.pdpdt.2015.07.170
67. Sunny SP, Agarwal S, James BL, et al. Intra-operative point-of-procedure delineation of oral cancer margins using optical coherence tomography. Article. *Oral Oncol*. May 2019;92:12-19. doi:10.1016/j.oraloncology.2019.03.006

68. Cals FL, Koljenovic S, Hardillo JA, Baatenburg de Jong RJ, Bakker Schut TC, Puppels GJ. Development and validation of Raman spectroscopic classification models to discriminate tongue squamous cell carcinoma from non-tumorous tissue. *Oral Oncol*. Sep 2016;60:41-7. doi:10.1016/j.oraloncology.2016.06.012
69. Hoesli RC, Orringer DA, McHugh JB, Spector ME. Coherent Raman Scattering Microscopy for Evaluation of Head and Neck Carcinoma. Article. *Otolaryngol Head Neck Surg*. Sep 2017;157(3):448-453. doi:10.1177/0194599817700388
70. Steybe D, Poxleitner P, Metzger MC, et al. Stimulated Raman histology for histological evaluation of oral squamous cell carcinoma. Article. *Clin Oral Investig*. 2023;27(8):4705-4713. doi:10.1007/s00784-023-05098-9
71. Barroso EM, Smits RWH, Schut TCB, et al. Discrimination between Oral Cancer and Healthy Tissue Based on Water Content Determined by Raman Spectroscopy. *Anal Chem*. Feb 17 2015;87(4):2419-2426. doi:10.1021/ac504362y
72. Fei BW, Lu GL, Wang X, et al. Label-free reflectance hyperspectral imaging for tumor margin assessment: a pilot study on surgical specimens of cancer patients. Article. *J Biomed Opt*. Aug 2017;22(8):7. 086009. doi:10.1117/1.Jbo.22.8.086009
73. Lu GL, Little JV, Wang X, et al. Detection of Head and Neck Cancer in Surgical Specimens Using Quantitative Hyperspectral Imaging. Article. *Clin Cancer Res*. Sep 2017;23(18):5426-5436. doi:10.1158/1078-0432.Ccr-17-0906
74. Halicek M, Dormer JD, Little JV, et al. Hyperspectral Imaging of Head and Neck Squamous Cell Carcinoma for Cancer Margin Detection in Surgical Specimens from 102 Patients Using Deep Learning. Article. *Cancers*. Sep 2019;11(9):16. 1367. doi:10.3390/cancers11091367
75. Long SM, McLean T, Valero Mayor C, et al. Use of Intraoperative Frozen Section to Assess Final Tumor Margin Status in Patients Undergoing Surgery for Oral Cavity Squamous Cell Carcinoma. *JAMA Otolaryngol Head Neck Surg*. Oct 1 2022;148(10):911-917. doi:10.1001/jamaoto.2022.2131
76. Lin K, Zheng W, Lim CM, Huang Z. Real-time in vivo diagnosis of laryngeal carcinoma with rapid fiber-optic Raman spectroscopy. *Biomed Opt Express*. Sep 1 2016;7(9):3705-3715. doi:10.1364/BOE.7.003705
77. Zhang LL, Wu YZ, Zheng B, et al. Rapid histology of laryngeal squamous cell carcinoma with deep-learning based stimulated Raman scattering microscopy. Article. *Theranostics*. 2019;9(9):2541-2554. doi:10.7150/thno.32655
78. Ramezani K, Tofangchiha M. Oral Cancer Screening by Artificial Intelligence-Oriented Interpretation of Optical Coherence Tomography Images. *Radiol Res Pract*. 2022;2022:1614838. doi:10.1155/2022/1614838
79. Heidari AE, Pham TT, Ifegwu I, et al. The use of optical coherence tomography and convolutional neural networks to distinguish normal and abnormal oral mucosa. *J Biophotonics*. Mar 2020;13(3):e201900221. doi:10.1002/jbio.201900221
80. Yang ZH, Shang JW, Liu CL, Zhang J, Liang YM. Identification of oral cancer in OCT images based on an optical attenuation model. Article. *Lasers Med Sci*. Dec 2020;35(9):1999-2007. doi:10.1007/s10103-020-03025-y

Development of an augmented reality system for tracheal intubation guidance of airway management

Grace T. Fei¹, Aimee W. Guo², Timothy Booth³,
Edgar Kiss⁴, Rami R. Hallac⁵, Andrew Anderson⁶, Zhiyue J. Wang³

¹Liberty High School, Frisco, Texas; ²The Hockaday School, Dallas, Texas; ³Department of Radiology, University of Texas Southwestern Medical Center, Dallas, Texas, ⁴Department of Anesthesiology, University of Texas Southwestern Medical Center, Dallas, Texas, ⁵Department of Surgery, University of Texas Southwestern Medical Center and Children's Health, Dallas, Texas; ⁶Department of Radiology, Children's Health, Dallas, Texas

ABSTRACT

Tracheal intubation is a crucial procedure performed in airway management to sustain life during various procedures. However, difficult airways can make intubation challenging, which is associated with increased mortality and morbidity. This is particularly important for children who undergo intubation where the situation is difficult. Improved airway management will decrease incidences of repeated attempts, decrease hypoxic injuries in patients, and decrease hospital stays, resulting in better clinical outcomes and reduced costs. Currently, 3D printed models based on CT scans and ultrasound-guided intubation are being used or tested for device fitting and procedure guidance to increase the success rate of intubation, but both have limitations. Maintaining a 3D printing facility can be logistically inconvenient, and it can be time consuming and expensive. Ultrasound-guided intubation can be hindered by operator dependence, limited two-dimensional visualization, and potential artifacts. In this study, we developed an augmented reality (AR) system that allows the overlay of intubation tools and internal airways, providing real-time guidance during the procedure. A child manikin was used to develop and test the AR system. Three-dimensional CT images were acquired from the manikin. Different tissues were segmented to generate the 3D models that were imported into Unity to build the holograms. Phantom experiments demonstrated the AR-guided system for potential applications in tracheal intubation guidance.

Keywords: Augmented reality (AR), tracheal intubation, user interface, image-guided intervention, airway management

1. INTRODUCTION

Tracheal intubation is a pivotal process due to its expectation to sustain life while performing necessary procedures. Also known as endotracheal intubation (ETI), tracheal intubation is a lifesaving process in which an endotracheal tube is inserted via the mouth of a patient into the trachea to ensure airflow through the tube [1]. The ETI procedure can occur either in or out of a hospital environment and comes with additional intrinsic difficulties. While there are a multitude of training programs targeting the difficult procedure of tracheal intubation, the methods are often limited and require more advanced technology to guarantee fully developed skill levels. It is therefore imperative to address this clinical challenge by more extensive technological research to enhance patient care. The research activities in this area have become increasingly active but are still inadequate to meet the challenge.

Currently, 3D printed models based on CT scans and ultrasound-guided intubation are being used or tested for device fitting and procedure guidance to increase the success rate of intubation [2-6], but both have limitations. Maintaining a 3D printing facility can be logistically inconvenient, and ultrasound-guided intubation can be hindered by operator dependence, limited two-dimensional visualization, and potential artifacts. The relative positions of the spine, head, and mandible can be drastically different during intubation and routine CT. In routine radiology scanning, the patients' head and neck assume a natural posture. During intubation, the head is tilted back, and the mouth is fully open. Therefore, the 3D model needs to be adjustable in positions and needs to be validated. The models need to be adjusted to allow head tilting relative to the C-spine and mandible opening relative to the skull. The airway anatomy needs to be adjusted according to the head and jaw positions. In addition, the airway needs to be modeled as a soft body which can be deformed in response to forces from laryngoscope and intubation tube.

Augmented reality (AR) technologies have a significant potential in the field of clinical study [7-9]. AR technologies for surgical applications continue to develop over time. The concept of involving real-world circumstances in a virtual environment is demonstrated through methods from a projected screen to a physical headset device [10]. Although augmented reality systems are extremely beneficial to physician training, AR technology is often difficult to incorporate with current systems, resulting in restricted user control. This project aims to increase the productivity and flexibility of AR systems in order to provide physicians with a more comprehensive observation of 3D models through the HoloLens 2 headset. Such improvements include increased modification options, color supply, and user personalization. With the refined AR system, physicians and patients alike will experience less stress, thus leading to broad acceptance and integration of the system. In accordance with tracheal intubation, AR systems have the potential to enhance trainee experiences through 3D visualization, resulting in accelerated developments in the field. While AR technology has the potential to teach medical procedures and serves as a tool for physicians performing minimally invasive surgery, it is envisioned to be a supplementary improvement for current clinical training methods rather than a replacement [11]. Zhao et al developed an AR framework to assist neonatal endotracheal intubation training [12]. A manikin and laryngoscope were used for the procedure. Their developed AR framework used multi-variate time-series data, a convolutional neural network, and the gradient-weighted class activation mapping to predict performance level and produced accessible evaluation of the ETI procedure. Ming et al. proposed the development of an augmented reality-assisted laryngoscopy system that has an attached live camera, improving visualization properties while adhering to a constant line-of-sight view [13]. The system includes a head-mounted device with augmented reality features. The researchers also carried out a pilot study with subjects, and the results indicate that the AR-assisted video laryngoscopy method is more efficient than traditional indirect technology in patients.

Overall, our project aims to address the challenges of building reliable digital models for simulating the intubation procedure, ultimately increasing the success rate of intubation, and improving patient outcomes. With the HoloLens 2 headset, an augmented reality system is developed to allow the overlay of intubation tools and internal airways on patients, providing real-time guidance during various interventional procedures.

2. MATERIALS AND METHODS

2.1 Phantom Models

A pediatric manikin phantom was used in this study (Figure 1). The phantom was scanned with computer tomography (CT) at UT Southwestern Medical Center. We constructed the digital models of the phantom from CT images of the phantom. The scanned CT DICOM images are then loaded into 3D Slicer to generate the digital 3D models.



Figure 1. The child manikin phantom used for the AR experiment. The phantom model displays the head and neck regions and was scanned using computer tomography (CT) to acquire DICOM images of the phantom.

After the DICOM images were loaded into 3D Slicer, the images are then cropped to remove unnecessary parts of the 3D images, such as the bed and background. Segmentation features in 3D Slicer are applied to segment the bone and tissue

of the DICOM images (Figure 2). We first used the threshold tools of 3D Slicer to differentiate between bone and soft tissue components of the phantom. Contrasting colors such as red and blue were initially used to differentiate between the tissue and bone segments. After obtaining the threshold minimum and maximum range values, we adjusted the material color and transparency to adhere to realistic visual effects. The finalized segmentation in 3D Slicer with tissue and bone components were then exported and saved as OBJ files to ensure compatibility with the Unity software. The OBJ file format preserves the 3D geometry, material, and visualization of the 3D Slicer segment.

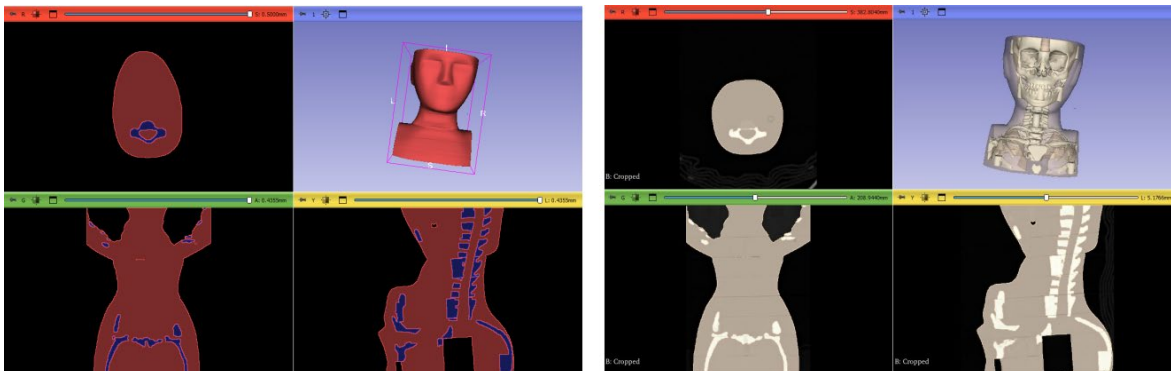


Figure 2. The bone and software tissue in the head and neck CT images were segmented using 3D Slicer. The segmented tissues are visualized in 3D Slicer using realistic material colors and tissue transparency.

2.2 Unity Platform and Mixed Reality Toolkit

The Unity editor version 2020.3.28f1 was used in this project. The HoloLens compatibility features of this version are crucial for later app deployment in the final steps. The Windows Build Support IL2CPP and Universal Windows Platform Build Support were also used in the implementation. A Universal Windows Platform (UWP) build setting in Unity is also required for this project (Figure 3). The UWP allows for a created Unity project to be combined or published among other Windows devices, in our case, Microsoft HoloLens 2. The Architecture was set to ARM64, which is a CPU processor architecture compatible with HoloLens 2 specifically.

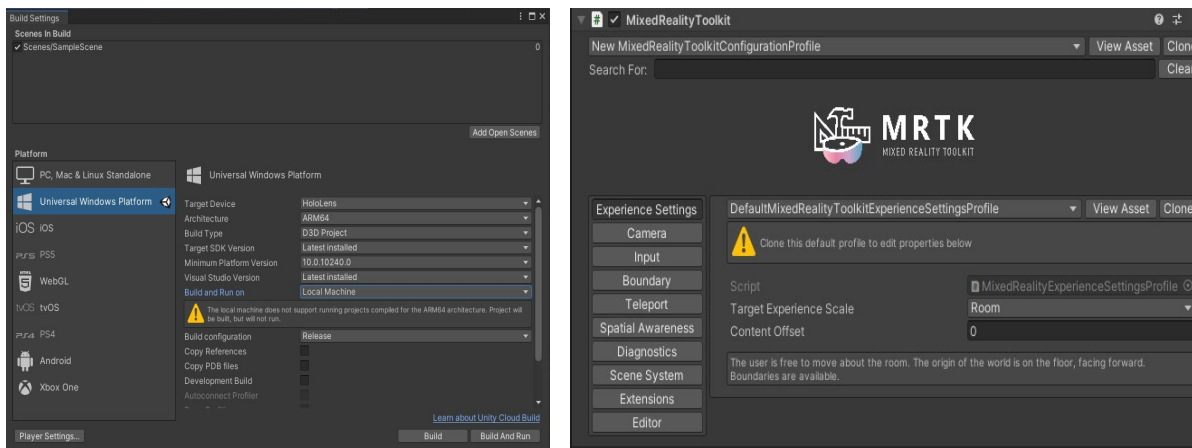


Figure 3: Universal Windows Platform and the Mixed Reality Toolkit in the Unity environment.

Mixed Reality Toolkit (MRTK version 2.8.3.0) works across multiple platforms and provides Microsoft features and components that support mixed reality (MR), virtual reality (VR), and AR app development in the Unity software. The Mixed Reality Feature Tool allows us to add and discover MRTK packages into creations. The required dependency that we validated and imported is the Mixed Reality Toolkit Standard Assets. The Unity OpenXR Plugin, eye gaze interaction, hand interaction, and motion control were used to permit user interactivity in the project development. The holographic remoting feature allows the visualization of 3D objects in the HoloLens prior to and without deployment for more efficient testing and troubleshooting of the Unity project.

The previously saved OBJ file from 3D Slicer is then imported into the Unity Project. Since our segmentation was saved and imported as an OBJ file, the tissue and bone subunits are automatically imported as children of the entire segmentation model. Certain MRTK components (box collider, constraint manager, object manipulator, and near interaction grabbable) were added to our segmented models for user interaction, intractability, and manipulation with the 3D object in the holographic remoting player and app deployment (Figure 4). Those components allow the object to be moved, scaled, and rotated by one-handed or two-handed input from the user. The near interaction grabbable component allows the 3D object to sense and respond to hand input motions nearby.

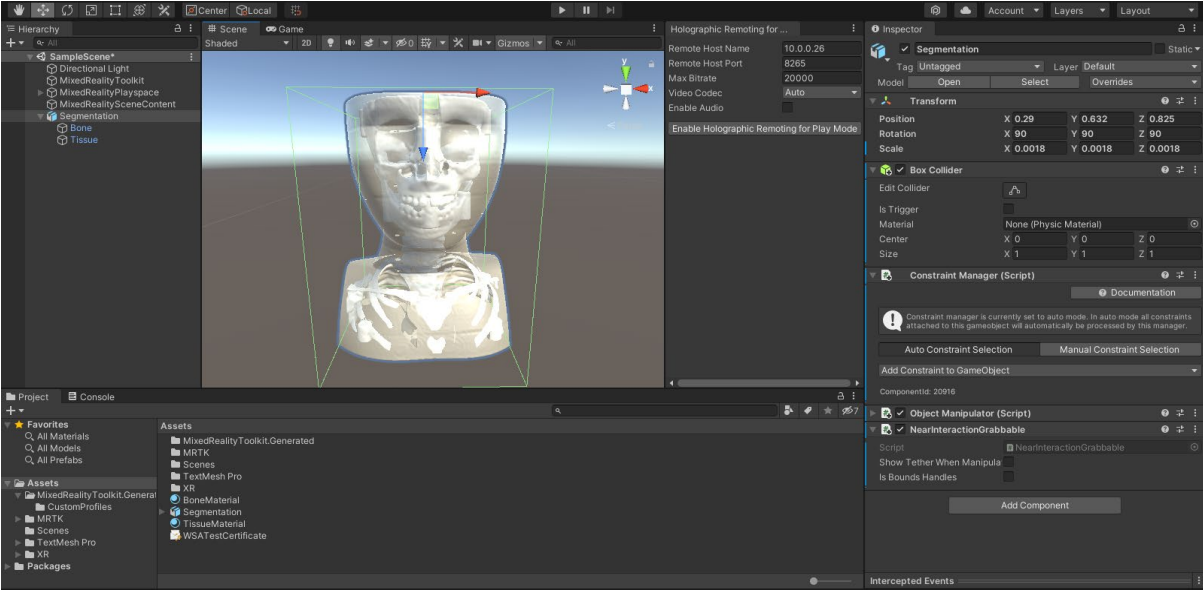


Figure 4: 3D segmented models in the Unity environment. The Mixed Reality Toolkit objects are imported under the Unity scene. The segmented bone and tissue components as well as other added components are shown to allow for user interaction and navigation.

2.3 Holographic Remoting and Deployment to HoloLens 2

To test our Unity project without final app deployment, the holographic remoting player was used to allow the user to view the 3D objects directly from the creation software Figure 5. The immersive view of the Unity project using holographic remoting supports user interaction qualities, such as object manipulation, movement, and rotation using hands.

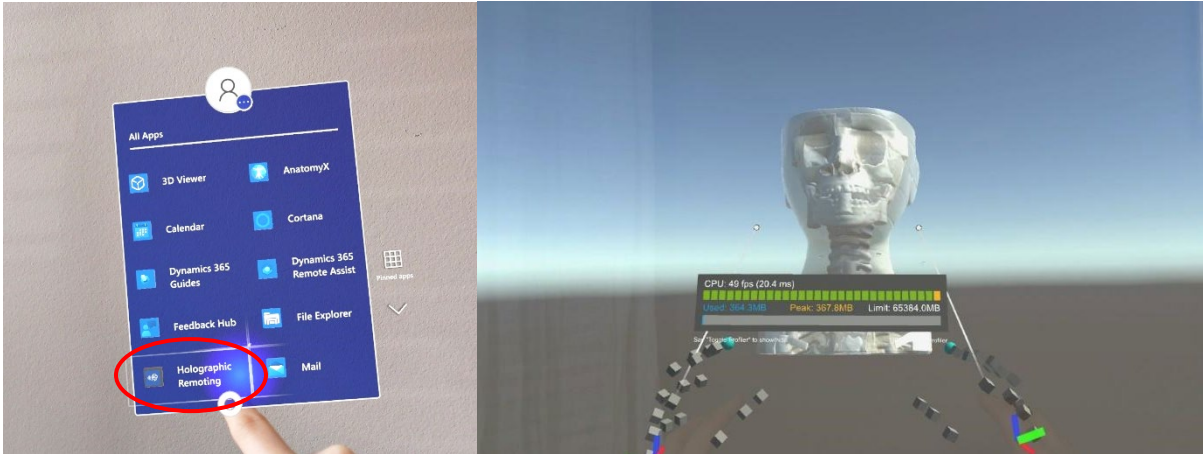


Figure 5. The use of the holographic remoting feature (left) and the HoloLens 2 view (right).

Once the Unity scene has been finalized and checked with Holographic Remoting, the 3D model is deployed directly

to the nearby HoloLens 2 device with Visual Studio (2022 version). This action establishes that the final deployed HoloLens app opens as a 3D immersive experience rather than a 2D window screen. After the deployment was completed in Visual Studio, the Unity project appeared as an application on the HoloLens 2 device headset. An alternative method of deploying our Unity models onto HoloLens 2 is to create and install an app package with the same Visual Studio code from the previously saved builds folder. Our initial method of direct deployment was a time-consuming process which required manual repetition for each device during app deployment. The alternative process results in an identical app as the direct deployment method but is ultimately more efficient as it does not require the HoloLens 2 to be awake throughout the entire process. Similar to the direct deployment method explained previously, it is important to set the HoloLens and computer connected to the same Wi-Fi signal to allow for connection and communication between the devices. Once the deployment is successful, the finalized application can now be found under the HoloLens applications section.

3. RESULTS

Spatial mapping in HoloLens 2 is an automatic process that uses external cameras on the device to determine the shapes and locations of nearby surrounding structures (Figure 6). The process is also known as spatial awareness and results in wireframe lines consistent with figures in the real-world environment. This representation of the real-world environment helps avoid collision and assists in merging the virtual and real worlds. However, the repeating lines can often result in the obstruction of 3D models or figures that need to be clearly viewed. Also, the spatial mapping feature in HoloLens 2 considerably slows down the AR system through the constant remapping of surroundings with each change in motion. As a result of such a problem, we were able to disable the spatial awareness system with the MixedRealityToolkit. Our resulting product is a HoloLens view with significantly reduced surrounding clutter and an increased headset speed. Alongside the improved scene clarity, these changes may also preserve the processing power of the HoloLens 2 headset and allow the device to focus on computational tasks that require more input. The final system was demonstrated in a phantom experiment (Figure 7) to showcase the feasibility of the augmented reality system for potential application in intubation guidance.

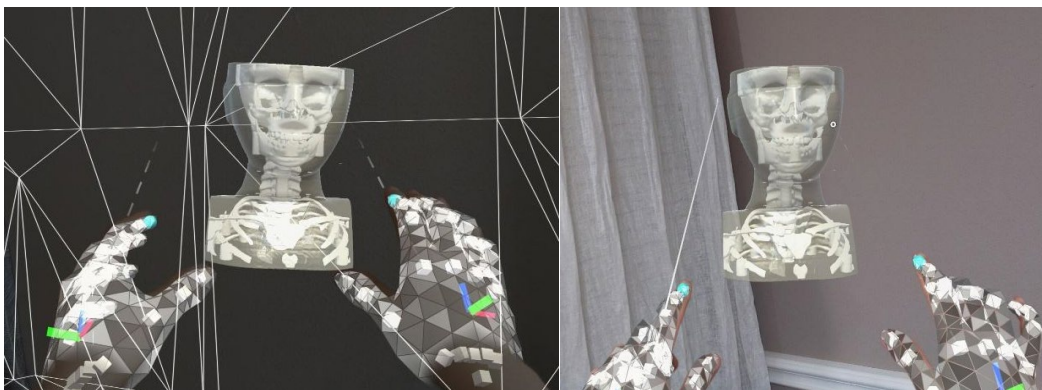


Figure 6. The Unity project deployed to HoloLens 2 in an environment with (*left*) and without (*right*) spatial mapping.

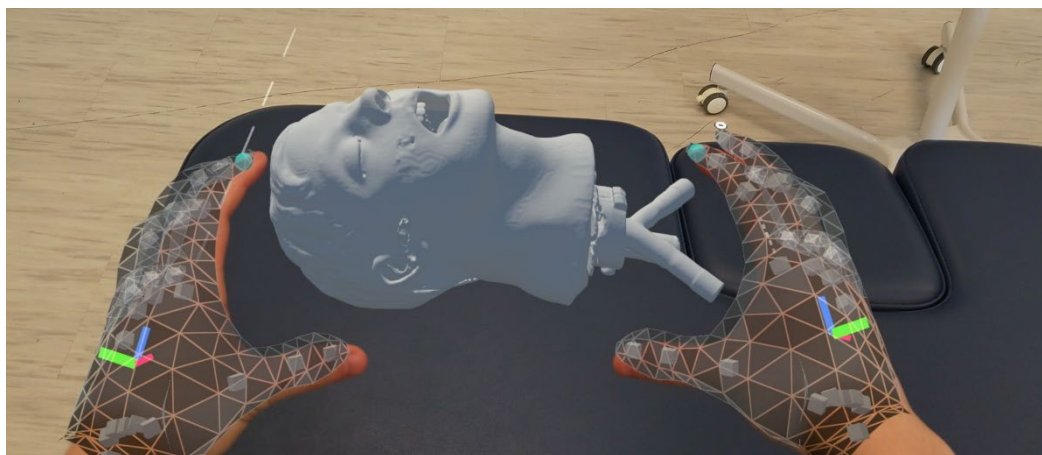


Figure 7. A demonstration of the AR system using a child manikin for potential applications in tracheal intubation procedures.

4. DISCUSSION AND CONCLUSION

We developed an augmented reality system that can be potentially used to improve clinician interactions in tracheal intubation for difficult airway management. Additional future developments include the addition of user interaction features within the AR scene, allowing adjustments to the transparency or RGBT values of the 3D model. These creations can be done using a C# script component in the Unity scene setup and would improve physician flexibility when working with the AR system. A transparency slider would assist in observing overlaps between the virtual and real worlds. The addition of color-adjusting sliders within the interface provides the physicians with more option variety in visualizing the 3D segmented model. Currently, 3D Slicer is used to crop and segment CT images of the head and neck. Future development includes automatic segmentation in the Unity platform. The Mixed Reality Toolkit provides the necessary features and components for holographic remoting testing and ranged manipulation of the 3D object in an AR environment.

REFERENCES

- [1] J. Rolland, L. Davis, F. Hamza-Lup *et al.*, "Development of a training tool for endotracheal intubation: distributed augmented reality," *Stud Health Technol Inform*, 94, 288-94 (2003).
- [2] J. Ock, E. Gwon, D.-h. Kim *et al.*, "Patient-specific and hyper-realistic phantom for an intubation simulator with a replaceable difficult airway of a toddler using 3D printing," *Scientific Reports*, 10(1), 10631 (2020).
- [3] D. Ormandy, B. Kolb, S. Jayaram *et al.*, "Difficult airways: a 3D printing study with virtual fiberoptic endoscopy," *Br J Oral Maxillofac Surg*, 59(2), e65-e71 (2021).
- [4] K. J. Kovatch, A. R. Powell, K. Green *et al.*, "Development and multidisciplinary preliminary validation of a 3D printed pediatric airway model for emergency airway front of neck access procedures," *Anesthesia and analgesia*, 130(2), 445 (2020).
- [5] Y. Liu, W. Ma, and J. Liu, "Applications of Airway Ultrasound for Endotracheal Intubation in Pediatric Patients: A Systematic Review," *J Clin Med*, 12(4), (2023).
- [6] M. Farrokhi, B. Yarmohammadi, A. Mangouri *et al.*, "Screening Performance Characteristics of Ultrasonography in Confirmation of Endotracheal Intubation; a Systematic Review and Meta-analysis," *Arch Acad Emerg Med*, 9(1), e68 (2021).
- [7] P. L. Dias, R. G. Greenberg, R. N. Goldberg *et al.*, "Augmented Reality-Assisted Video Laryngoscopy and Simulated Neonatal Intubations: A Pilot Study," *Pediatrics*, 147(3), (2021).
- [8] A. Alismail, J. Thomas, N. S. Daher *et al.*, "Augmented reality glasses improve adherence to evidence-based intubation practice," *Adv Med Educ Pract*, 10, 279-286 (2019).
- [9] L. Davis, Y. Ha, S. Frolich *et al.*, "Augmented reality and training for airway management procedures," *Stud Health Technol Inform*, 85, 121-6 (2002).
- [10] J. Sutherland, J. Belec, A. Sheikh *et al.*, "Applying modern virtual and augmented reality technologies to medical images and models," *Journal of digital imaging*, 32, 38-53 (2019).
- [11] K. F. Kerner, C. Imielinska, J. Rolland *et al.*, "Augmented Reality for teaching endotracheal intubation: MR imaging to create anatomically correct models," *AMIA Annu Symp Proc*, 2003, 888 (2003).
- [12] S. Zhao, X. Xiao, Q. Wang *et al.*, "An Intelligent Augmented Reality Training Framework for Neonatal Endotracheal Intubation," *Int Symp Mix Augment Real*, 2020, 672-681 (2020).
- [13] M. Qian, J. Nicholson, D. Tanaka *et al.*, "Augmented reality (AR) assisted laryngoscopy for endotracheal intubation training," *Virtual, Augmented and Mixed Reality. Applications and Case Studies: 11th International Conference, VAMR 2019, Held as Part of the 21st HCI International Conference, HCII 2019, Orlando, FL, USA, July 26–31, 2019, Proceedings, Part II* 21, 355-371 (2019).